CENTRO DE INVESTIGACIONES EN ÓPTICA, A.C.

Temperature Measurement of Transient Events by Ray Deflection Methods (Definitive Version. Includes suggested changes by reviewers)

MSc. Alan David Blanco Miranda

Thesis work submitted to Centro de Investigaciones en Optica A. C.

for the degree of

Doctor of Sciences (Optics)

Accepted on the recommendation of:

Dr. Bernardino Barrientos García, supervisor

Members of the Committee:

Dr. Luis Mariano Cerca Martínez, reviewer

Dr. Adrián Martínez García, reviewer

Leon, Gto., September 9th, 2016.

Dedicatory

I dedicate this work to…

To my parents
Eulogio Blanco H. and Magdalena Miranda B.,
For their love, support, comprehension and faith into me.
Thank them for everything that they gave me, all the sacrifices
that they made in order that I could achieve all my personal and professional objectives.
This is a triumph because of them.

To my wife
Alejandra Sánchez H.,
Who always gave me her friendship, supported me,
encouraged me to achieve this personal objective, and
for being my life companion, to arrive to my life for give me
all her love and giving me the opportunity to made a family.

To my daughter
Aline Blanco Sánchez,
For her unconditional and pure love, her creativity,
her jokes and being my personal motivation every day to always go forward
and achieve every goal.

To my sisters, Diana and Nancy
for always being supporting me, specially in the difficult moments.
for having encouraged me to achieve this personal objective.

Acknowledgments

I would like to thank my parents for their friendship, encouragement and caring over all these years, for always being there for me through thick and thin and without whom this project would not be possible. I would also like to thank my grandparents, aunts, uncles and cousins for their understanding and support throughout all these years.

I would also like to acknowledge my dissertation supervisor Dr. Bernardino Barrientos for his insight, support and sharing of knowledge that has made this Thesis possible.

I am indebted to Dr. Amalia Martínez, Dr. Carlos Pérez, Dr. Miguel Mora González, Dr. Adrián Martínez and Dr. Mariano Cerca for acting as co-examiners of my doctoral work and for their valuable input.

Also, I would like to thank Centro de Investigaciones en Óptica A.C. (CIO), institution which gave me the opportunity to develop my research hability and provided me all the available media to achieve this goal in my life. Also, it gave me the chance to know wonderful people whom encouraged me to go forward and always go deep in research items to solve practical cases and generate new knowledge.

I would like to thank the Consejo Nacional de Ciencia y Tecnologia (CONACyT), for its economical

support given by the scholarship with register 316554, and without which this research work wouldn't be possible.

Special acknowledgment to Action Training CTC to encourage me to achieve this goal and remember me that every real goal in my life depends on me and my being, it drives me to achieve everything I can imagine.

Last but not least, to all my friends and colleagues that helped me grow as a person and were always there for me during the good and bad times in my life. Thank you.

To each and every one of you,

Thank you

MSc. Alan David Blanco Miranda

Abstract

In this work, we report on a performance comparison between two experimental techniques, background-oriented schlieren (BOS) and fringe deflection (FD), when used for temperature measurement of phase objects. Both techniques are capable of measuring gradients of temperature fields, by employing a background image, which is imaged by a camera. The object phase under study is placed between the background and the camera. Some features of BOS and FD, such as robustness and spatial resolution, are studied. First, we give an analysis of each technique to find the optimum parameters for numerical processing. Then, by numerical simulations and experimental work we analyze their performance. The results show that FD, for typical associated displacements, was larger than that obtained by BOS. For relatively small and large displacements (0.5 pix and 7.5 pix, respectively) of the spatial structures of the background, errors tended to be rather large for both techniques. This is an important result since, currently, BOS is predominantly used for most of the practical applications where measurement of temperature fields is involved. In BOS, in order to have results with enough accuracy, it is necessary to count with specialized software or buy expensive licenses (for example, any of the Digital Image Correlation software licenses). Unlike this, the software for FD is relatively simple (as long as no complex phase unwrapping algorithms are required), with the phase extraction method (the Fourier method) being the most extensive-programming part, but which can be programmed right away. This is important for industry, since costs can be reduced.

Experimentally, two different sizes of the region of observation were employed. BOS and FD were implemented either separately or simultaneously (this latter variation was carried out by encoding the signals for each technique on the RGB channels of color images). From the results, it is apparent that the performance of FD, considering spatial resolution, again is slightly better than that of BOS. A similar result was found for images with low contrast.

In the last part of the thesis we present an application related to the analysis of a Helmholtz resonator, where FD is used. This type of device is currently being tested as a refrigeration system. In this case, a synthetic pulsed jet is produced, and it is directed onto a surface to be cooled; for example, the surface of an electronic chip.

This thesis work could be of interest to readers in the areas of fluid mechanics, plasma physics and optical engineering, and to any person developing optical instrumentation for industry.

Contents

List of Figures

1

Introduction

Contents

In this chapter, we introduce the main proposals of the thesis work. Besides, we briefly describe the motivation of the work and point out the importance of temperature measurement. Then, an overview of the analyzed techniques is given. After that, the main objectives of the work are presented. Finally, in section 1.4, the content of this thesis is included.

1.1 Motivation

In the study of fluid flows, the assessment of temperature and density are of great importance. One of the preferred methods that is being used for that purpose is background-oriented schlieren (BOS), where a background image is used for the measurement of displacement, in pixels. The displacement is related to the apparent movement of the spatial structures of the background as a phase object — object to be studied – is introduced in the setup. It is common that the structures of the background consist of a set of randomly located spots. In this case, the displacement maps arising from the comparison between reference (with no object) and displaced (with phase object) images, are computed via digital image correlation (DIC). DIC is quite a robust method, but generally is based on complex numerical algorithms, in particular when sub pixel accuracy of displacement is to be achieved. In this work, we carry out a comparison study between DIC and Fringe Deflection (FD). FD is a variation of the classic BOS, where the spots background is replaced by a Ronchi grating — in these circumstances, the displacement field is calculated by optical phase methods, such as the Fourier transform method —. Unlike DIC, FD incorporates simple algorithms and, as shown in this document, yields displacement measurements with slightly larger accuracy. One application of FD included in this work is the measurement of temperature through the ray equation and the Gladstone-Dale equation. A case study is a synthetic air jet produced by a Helmholtz cavity. This device recently has been used for the cooling of parts subjected to thermic load, such as microprocessors.

1.2 Analyzed techniques

The use of optical techniques for the temperature measurement has advantages over other methods, for example thermocouples, since they do not introduce disturbances in the object under study. They are also full field, meaning that measurements of a whole region can be realized.

As mentioned above, two optical methods for temperature measurement, Fringe Deflection (FD) and Background Oriented Schlieren (BOS) are analyzed in this work. Fringe Deflection is a variation of the classic BOS. Both techniques are capable of measuring displacement fields which are proportional to the gradient of refractive index distributions within a region of observation. In both techniques, a synthetic background (a pattern of straight fringes with sinusoidal profile for FD and a pattern of randomly-located spots for BOS) is imaged by a camera. The object under analysis is placed between the background and the camera. Two images are captured, with and without the object. These images are the reference image and the displaced image, respectively. As the object is introduced, the spatial structures of the background are displaced according to the deflection of the corresponding bundle of rays that propagate through the object. The reference and the displaced images are then compared, and the displacements calculated.

Displacement vector fields corresponding to ray deflections can be numerically integrated to obtain the spatial distribution of the projected refractive index, which may be related to density or concentration variations. It is worth noting that unlike BOS, FD has not been used extensively in these kind of applications.

.

1.3 Thesis Aim

The main objective of this work is to evaluate the performance of FD and BOS through both numerical simulations and experimental images. Two features of the used images serve for the evaluation: The spatial resolution and the sensitivity to image blur. The evaluation is done when the techniques are used for the measurement of gradients of temperature in phase objects (exit of the gas nozzle). Another objective is the study of the dynamical behavior of a Helmholtz cavity. This cavity produces a synthetic air jet that when interacts with hot surfaces, an efficient cooling process takes place.

The hypothesis of this work is to show that the technique of FD has such sensitivity as BOS technique and can be used for analysis of transient phenomena with high temperature variations.

1.4 Thesis structure

Chapter 2 includes the theoretical background of both techniques (FD and BOS). We describe the theory of FD and BOS, specifically the mathematical development to obtain variables such as the phase difference, the refractive index gradient and the temperature, and we show a numerical example in order to illustrate the followed procedure and the meaning of each mathematical expression. Also, a brief conclusion is given, commenting the main advantages and disadvantages of each technique.

Then, in Chapter 3 we report results of numerical simulations which allow us to select the optimal parameters for both techniques; a phase object with a circular Gaussian distribution of refractive index is considered for both techniques. After that, we evaluate the spatial resolution of FD and BOS, and we show an analysis of the tolerance to low contrast of images.

In the Chapter 4, we repeat the evaluation done in Chapter 3, but in this case, experimental images are employed. The images are related to the measurement of gradients of temperature, which correspond to the exit jet from a combustion nozzle. We firstly implement the two techniques separately. Similar experimental conditions are maintained for both (object to background distance, exposure time, lens parameters, f-number, gas pressure). Displacement maps are measured and the results are compared. For a better comparison of BOS and FD, a setup that warrants simultaneity of the measurements through both techniques is employed. In this case, the information needed by BOS and FD is encoded in the RGB signal of a color image. By displaying this color image on a monitor, it can be recorded by a color camera. The images corresponding to each color channel of the recorded images are then available for analysis.

Results of the evaluation of the spatial resolution are then given. This evaluation comprises the analysis of a small depression, which is formed at the exit of the gas nozzle. For this analysis, two different sizes of the region of observation are considered. Fringe deflection and BOS are applied either separately or simultaneously. Finally, the sensitivity of the techniques to blur is reported.

An experimental application is reported in Chapter 5, where we present an application related to the analysis of a Helmholtz resonator, where FD is used. This type of device is currently being tested as a refrigeration system. In this case, a synthetic pulsed jet is produced, and it is directed onto a surface to be cooled.

Finally, in Chapter 6 we give the general conclusions of the work. Besides, we comment on possible future works.

2

Theory of Background-Oriented Schlieren and Fringe Deflection

Contents

The theoretical basis of the two techniques used in this work are described in this chapter. The trajectories of the rays are obtained through Fermat´s principle. The corresponding ray deviations —deflections— are calculated in different forms by the two techniques: FD and BOS. In FD, the displacements are obtained through phase extraction methods and in BOS, by digital image correlation. BOS and FD are based on the same principle: the deflection of rays when passing through a phase object (transparent object).

Both techniques use a background which is imaged by a camera. In BOS, the background contains spots randomly located and in FD, a set of parallel straight fringes (Ronchi grating).

2.1 Fermat´s Principle

A modern formulation of this principle states that the trajectory traveled by light going from one point to another is such that the time it takes is stationary with respect to variations of the possible paths. Mathematically this is expressed as follows.

The time it takes light to travel a distance s in a given medium is $t = \frac{s}{v}$, where s is distance and v the speed of light in the medium, which is assumed to be constant throughout the medium, regardless of the direction of travel. Defining the refractive index as $n = \frac{c}{v}$, where c is the speed of light in vacuum, then [1] - [2]

$$t = \frac{sn}{c} \tag{2.1}$$

A medium in which the refractive index depends on the position $n = n(s)$ was taken, then we can estimate that a differential element ds is traversed in a lapse of time $dt = \frac{n}{c}ds$; the total time between two points E and F is

$$t = \frac{1}{c}\int_{E}^{F} n(s)\, ds \tag{2.2}$$

Then, by Fermat's principle we find the extreme values of the function as

$$\delta \int_{E}^{F} n\left(s\right) ds = 0 \tag{2.3}$$

where δ is a constant.

2.2 Ray Deflection

By solving Eq. (2.3), the propagation of a ray through an inhomogeneous phase object can be obtained as, [3]

$$\frac{d}{ds}\left(n\frac{d\vec{r}}{ds}\right) = \nabla n, \tag{2.4}$$

where $\vec{r}$ is the ray position vector, $n(x, y, z)$ is the distribution of the index of refraction and s is the arc length parameter which depends of the direction of propagation z. By considering that the ray propagates paraxially in the z-direction, Eq.(2.4) can be decomposed into two equations, [4]

$$\frac{d^2x}{dz^2} = \frac{1}{n}\frac{\partial n}{\partial x}, \tag{2.5}$$

and a similar expression for the y-curvature. By integrating Eq.(2.5) once with respect to z, the angular deflections of the ray produced by the phase object at (x, y) can be calculated as (see Fig.(2.1) for the definition of some variables)

$$\theta_x = \left(\frac{dx}{dz}\right)_{z_2} = \frac{\Delta x}{D} = \frac{1}{n_0}\int_{z_1}^{z_2}\left(\frac{\partial\left(\Delta n\right)}{\partial x}\right)_{\vec{r}} dz, \tag{2.6}$$

$$\theta_y = \left(\frac{dy}{dz}\right)_{z_2} = \frac{\Delta y}{D} = \frac{1}{n_0}\int_{z_1}^{z_2}\left(\frac{\partial\left(\Delta n\right)}{\partial y}\right)_{\vec{r}} dz, \tag{2.7}$$

where $n\left(x, y\right) = n_0 + \Delta n\left(x, y\right)$ and it is replaced in the denominator by n_0, which is the index of refraction of the reference state and $\Delta n\left(x, y\right)$ is the local variation of the refractive index with respect

to n_0, since in most practical cases $n \approx n_0$; D is the object-to-background distance, and Δx and Δy correspond to the apparent displacement of an image point due to the presence of the object, in the x- and y-directions, respectively. Also, the slopes of the ray, $(dx/dz)_{z_1}$ and $(dy/dz)_{z_1}$, at the entrance of the observation region have been assumed to be zero. Once the apparent displacements are measured, the distribution of the projected refractive index can be obtained.

If the variations in the refraction index arise from changes in temperature, then the projected temperature field may be computed by using a combination of the Gladstone-Dale equation and the equation for ideal gases at constant pressure, [6]- [8]

$$T = T_0 \frac{n_0 - 1}{n - 1}, \tag{2.8}$$

where T_0 is the temperature of the reference state for a certain point.

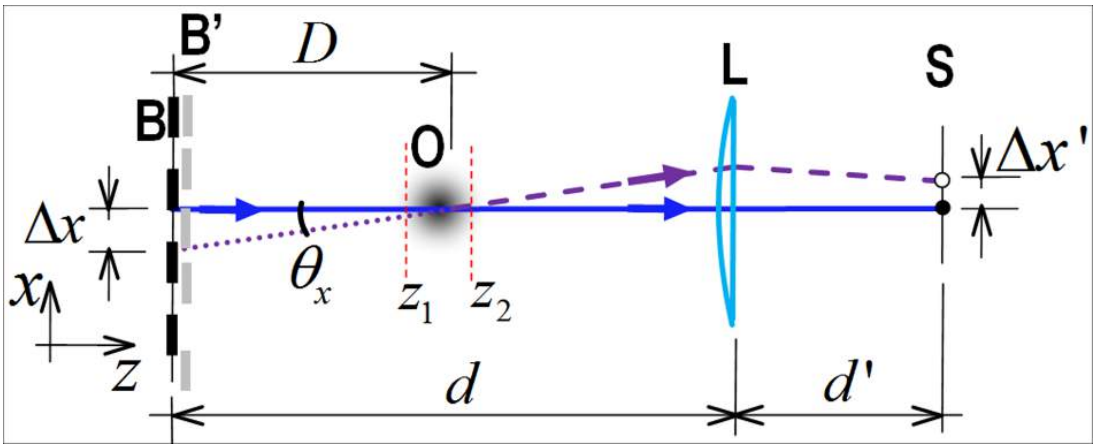

Fig. 2.1. Ray deflection caused by a phase object. After introducing the object O (red dotted lines), the blue ray is deflected along the direction of the purple ray. The background B and the camera sensor S are at distances d and d' from the imaging lens L, respectively.

In order to evaluate and contrast the performance of FD and BOS, an optical setup as the one depicted in Fig. 2.1 is implemented. In this figure, the size of the phase object O is indicated by the red dashed lines z_1 and z_2 . B and B' correspond to the position of the background pattern before and after the incorporation of the object, D is the object-to-background distance, and θ_x is the deflection angle, which is directly related to the apparent displacement Δx of an image point due to the presence of O. In addition, L stands for the imaging lens and S for the sensor plane.

Measured values of the angular deflection via Eqs. (2.6-2.7) corresponds to lines-of-sight integrated values of the refractive index. To recover the corresponding three dimensional distribution of the refraction index, standard tomographic techniques are used. [9]

For the special case of a Gaussian distribution of the refractive index, this one-to-one correspondence is straightforward. The local variation of the refractive index is given by

$$\Delta n = -\Delta n_0 \exp\left(-C\frac{y}{L_y}\right) \exp\left[-\frac{(x-x_0)^2 + (z-z_0)^2}{r_0^2}\right], \tag{2.9}$$

where Δn_0 is the maximum variation in the refraction index at the center of the phase object, r_0 and (x_0, y_0) are the radius and the coordinates of the center of the circular Gaussian function respectively, and L_y is the vertical size, in the y-direction, of the observation region. This function resembles the plume from a candle and is shown in Fig. (2.2a). The factor C in the first exponential term is a constant used to modify the rate of change of the refractive index in the y-direction. Inserting Eq. (2.9) into Eq. (2.6), the horizontal displacement function projected on the xy-plane of a sensor was obtained.

$$\Delta x = \frac{\sqrt{\pi}\, r_0 D}{n_0}\frac{\partial \Delta n'}{\partial x} = \frac{2\sqrt{\pi}\Delta n_0 D}{n_0 r_0}(x-x_0)\exp\left(-C\frac{y}{L_y}\right)\exp\left[-\frac{(x-x_0)^2}{r_0^2}\right], \tag{2.10}$$

which is a Gaussian function as well, where $\Delta n' = -\Delta n_0 \exp\left(-Cy/L_y\right)\exp\left[-(x-x_0)^2/r_0^2\right]$ is a function with no dependence in z. Note that the original radius of the Gaussian is preserved, and that the

effect of the line integration corresponds to a constant given by $\sqrt{\pi}r_0$ – the object size was assumed fully contained by the region of observation: $L_x > 4r_0$, with L_x being the size of the region in the x-direction. Therefore, if the measured profile for the displacements along the x-direction, for a particular y_0, happens to be the derivative of a Gaussian function, then $\frac{\partial \Delta n'}{\partial x}$ can be readily obtained by the first equality of Eq. (2.10), and hence, the use of any de-projection algorithm is avoided.

The vertical component of displacement, Δy, can be similarly found,

$$\Delta y = \frac{\sqrt{\pi}r_0 D}{n_0}\frac{\partial \Delta n'}{\partial y} = \frac{\sqrt{\pi}C\Delta n_0 r_0 D}{n_0 L_y}\exp\left(-C\frac{y}{L_y}\right)\exp\left[-\frac{(x-x_0)^2}{r_0^2}\right], \qquad (2.11)$$

Factor C may be selected so that the maximum apparent displacements in the x- and the y-directions are equal. In Fig. 2.2(b), a typical displacement function obtained by Eqs.(2.10) and (2.11) is shown. When this field is added to the positions of the spatial structures of a reference image, it yields the displaced image that can be used for numerical simulation purposes. These images can be analyzed by BOS and FD to recover the displacement field, and performance comparison can be done. For comparison purposes, the computation of the distribution of the refractive index is not necessary, but only the displacement maps. Displacement maps are calculated through Fourier transform correlation in BOS and through a Fourier phase-extraction method [10] in FD.

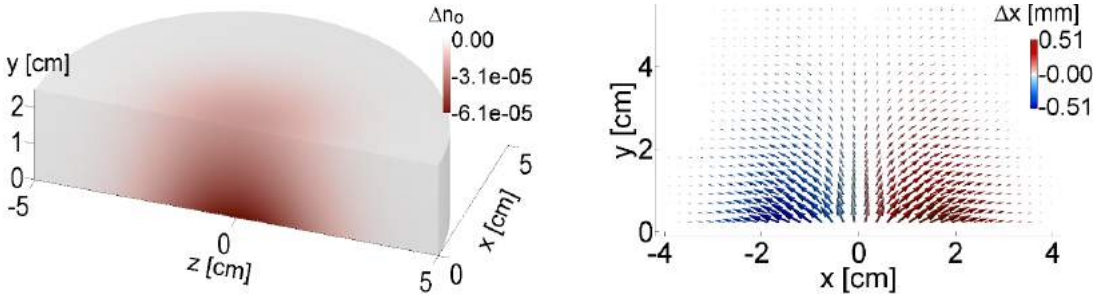

Fig. 2.2. Simulated plume. (a) Three-dimensional distribution of the variation of the index of refraction and (b) resulting displacement field at background plane. Maximum of displacement of Δx and Δy is $0.51\ mm$ or, equivalently, $2.5\ pixels$ for an image of 448x448 pixels.

2.3 Back-ground oriented schlieren

Flow visualization techniques for determination of density gradients are called schlieren techniques and they can be subdivided into different methods, for example, the Toepler method and focus method [11]. The technique described in this section will be referred to as BOS technique.

In BOS, the background images are formed by a set of randomly positioned particles. The profile of the particles follows a Gaussian function, and they are positioned according to a Sobol algorithm [12]. The relative displacement between the reference and displaced images can be obtained by cross correlation of corresponding subimages [13]- [14]. The distributions of intensity for particle subimages related to the images with and without object are $I_2(x, y)$ and $I_1(x, y)$, respectively. The displaced image can be expressed as $I_2(x, y) = I_1(x - \Delta x, y - \Delta y)$. The displacements $(\Delta x, \Delta y)$ can be found by means of the two-dimensional correlation function defined as

$$h(\Delta x, \Delta y) = \int_{-\infty}^{\infty} \int_{-\infty}^{\infty} I_1(x, y) I_2(x - \Delta x, y - \Delta y) dx dy, \tag{2.12}$$

which can be obtained through the Fourier transform,

$$h(\Delta x, \Delta y) = \Im^{-1} \left\{ F_1(f_x, f_y) F_2^*(f_x, f_y) \right\}, \tag{2.13}$$

where $F_1(f_x, f_y)$ and $F_2(f_x, f_y)$ denote the Fourier transform of I_1 and I_2, respectively. The inverse Fourier transform operator is indicated by $\Im^{-1}\{\}$, and the frequency domain variables by (f_x, f_y). The position of the maximum of the correlation map defines directly the unknown displacements. Subpixel resolution of the displacements can be achieved by fitting either Gaussian [15] or paraboloidal [16] functions to the region that contains the maximum peak of the correlation map.

In Figure 2.3 the image is displayed with randomly generated particles, greenish blue particles are shown in the reference positions, while red, the displaced particles. In Figure 2.3(b), subimages in which

the region under analysis is divided are shown.

For this example, displacements in two orthogonal directions are given, i.e. as if it were a rigid body motion for the entire set of particles that make up each subimage.

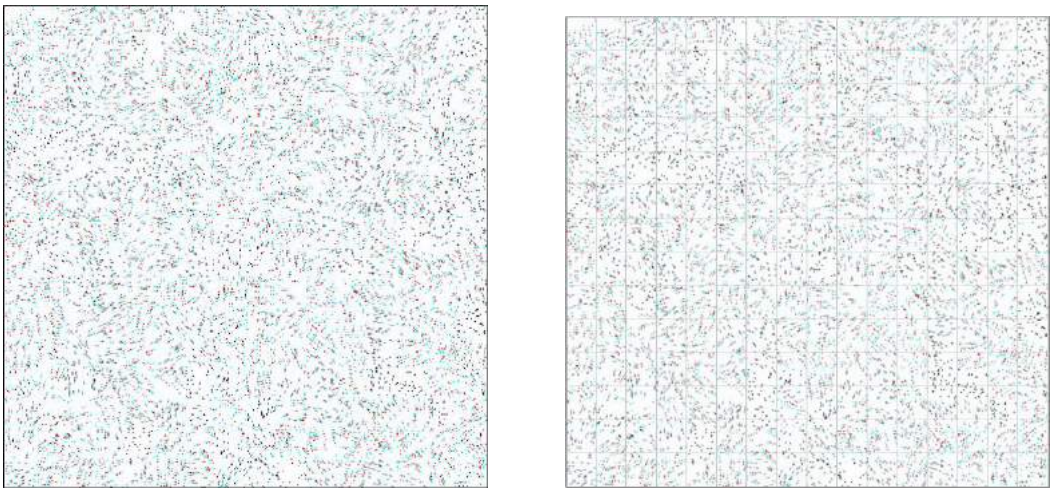

(a) (b)

Fig. 2.3. BOS generated image; a) reference positions (blue-green), displaced (red); b) Subimages.

The displacement between images could be calculated by using the Fourier transform method. Once the correlation for each pair of subimages is obtained, the location of the correlation peak for this example is calculated by the Gaussian interpolation method, which produces results with less error compared to the theoretical values of displacement.

The comparison between the displacements retrieved (Δx_r) and theoretical (Δx_t) is shown in Figure 2.4. Finally, the total error for this numerical simulation, taking into account the theoretical and retrieved movements, is calculated by the following expression,

$$\sigma_t = \sqrt{\frac{\sum_{i=1}^{N_s} \left(\Delta x_{r_i} - \Delta x_{t_i}\right)^2 + \sum_{i=1}^{N_s} \left(\Delta y_{r_i} - \Delta y_{t_i}\right)^2}{N_s}}, \tag{2.14}$$

where N_s denotes the number of subimage.

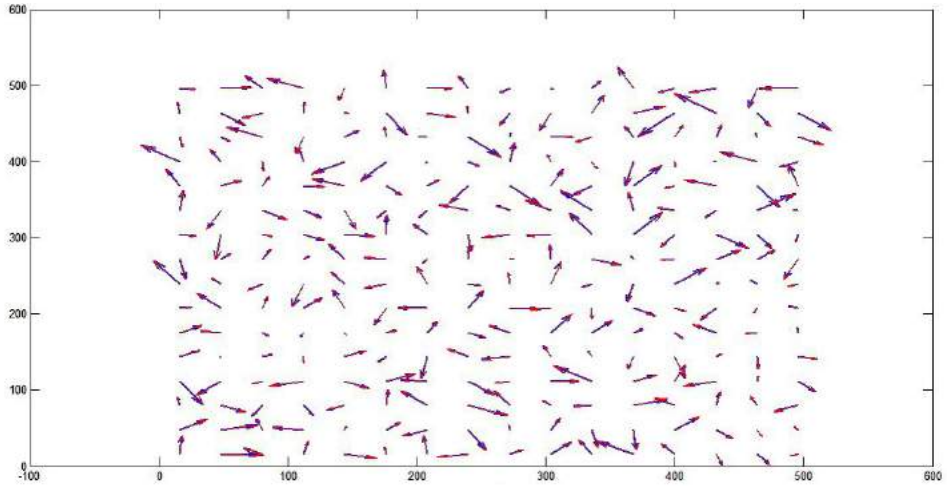

Fig. 2.4. Theoretical displacements (red) and retrieved displacements (blue). Horizontal axis is in pixels, vertical axis is in pixels.

The total error obtained for this example is $0.07\ pixels$ which equals $0.17\ \%$. Gradients in the refractive index must be retrieved for both spatial directions via Eqs. (2.6) and (2.7), to finally obtain the temperature changes given by Eq. (2.8).

2.4 Fringe Deflection

Fringe deflection is well suited for the calculation of in-plane displacements such as those involved in deflection of rays [17]. In this case, the background synthetic image is constituted by a pattern of straight sinusoidal fringes. Deviations from straightness of the fringes, for the displaced image, may be in the range of a fraction of the period of the grating. The deviations correspond to the displacement of each point forming a fringe. As displacements cannot be measured along the direction of the fringes, an additional crossed grating must be incorporated in order to have sensitivity to two mutually perpendicular directions [18]. The displacements can be calculated as follows. For background images composed of only one grating, oriented along the vertical direction, the reference image may be expressed by [19], [20]

$$I_1(x,y) = a(x,y) + b(x,y)\cos(2\pi f_0 x + \phi_{ref}), \tag{2.15}$$

where $a\,(x,y)$ is the background illumination, $b\,(x,y)$ the modulation term, f_0 a carrier frequency that allows us to use the Fourier method for automatic phase calculation, and ϕ_{ref} is a phase term that accounts for aberration effects. Likewise, the displaced image can be expressed as

$$I_2(x,y) = a(x,y) + b(x,y)\cos(2\pi f_0 x + \phi_{ref} + \Delta\phi), \tag{2.16}$$

with $\Delta\phi\,(x,y)$ being the phase resulting from deviations in the straightness of the fringes, after introducing the object. The arguments of Eqs. (2.15) and (2.16) can be calculated by applying the Fourier phase-extraction method. For example, for the reference image, Eq. (2.11) should be written as [10]

$$I_1(x,y) = a(x,y) + \frac{1}{2}b(x,y)\ \exp\left(i2\pi f_0 x\right)\exp\left(i\phi_{ref}\right) + \frac{1}{2}b^*(x,y)\ \exp\left(-i2\pi f_0 x\right)\exp\left(-i\phi_{ref}\right). \tag{2.17}$$

Applying the Fourier transform to Eq. (2.17), yields

$$I_F(f_x,f_y) = A(f_x,f_y) + B(f_x - f_0, f_y) + B^*(-f_x - f_0, f_y), \tag{2.18}$$

where $A\left(f_x, f_y\right) = \Im\{a\left(x, y\right)\}$ and $B\left(f_x, f_y\right) = \Im\left\{\frac{1}{2}b\left(x, y\right)\exp\left(i2\pi f_0 x\right)\exp(i\phi_{ref})\right\}$.

Next, a band-pass filter is applied to Eq. (2.18) to isolate one of its side lobes (centered at the carrier frequency f_0), which gives

$$I_{FP}(f_x, f_y) = B(f_x - f_0, f_y). \tag{2.19}$$

Finally, inverse Fourier transform of Eq. (2.19) is taken, yielding

$$\begin{aligned}\Im^{-1}\left\{B(f_x - f_0, f_y)\right\} &= \Im^{-1}\left\{\Im\left\{\frac{1}{2}b(x, y)\exp(i2\pi f_0 x)\exp\left(i\phi_{ref}\right)\right\}_{f_x - f_0, f_y}\right\} \\ &= \frac{1}{2}b(x, y)\exp\left[i\left(2\pi f_0 x + \phi_{ref}\right)\right] \\ &= C(x, y) + i\, S(x, y)\end{aligned}, \tag{2.20}$$

where $C(x, y) = \frac{1}{2}b(x, y)\cos\left(2\pi f_0 x + \phi_{ref}\right)$ and $S(x, y) = \frac{1}{2}b(x, y)\sin\left(2\pi f_0 x + \phi_{ref}\right)$. Therefore, the reference argument can be obtained by $2\pi f_0 x + \phi_{ref} = \tan^{-1}\left[S(x, y)/C(x, y)\right]$. In a similar way, the argument of the displaced fringe pattern, $(2\pi f_0 x + \phi_{ref} + \Delta\phi)$, can be calculated; then, the desired phase term can be finally obtained by subtracting the latter two arguments [21],

$$\Delta x = p\frac{\Delta\phi}{2\pi}, \tag{2.21}$$

where $p = 1/f_0$ denotes the period of the grating.

Below is an example of FD where sensitivity is to two orthogonal directions. This is done by using a cross grating, which includes two gratings perpendicular to each other.

The first thing to do is to generate an image intensity distribution with a known carrier frequency for both crossed gratings; in this case, $32\ pixels$ in the horizontal direction and $25.6\ pixels$ in the vertical direction, in a $1280 \times 1024\ pixels$ region as shown in Fig. 2.5(a).

For this case, the known phase distribution is a parabolic distribution given by the following expression

$$\Delta\phi_{m,n} = \frac{2\pi}{p}\left[\left(\frac{x_n}{s_x}\right)^2 + \left(\frac{y_m}{s_y}\right)^2\right], \tag{2.22}$$

Where $\Delta\phi$ is the modulating phase, p is the period of the grating, x_n are the values of the paraboloid in x-direction, s_x is the width of the observed region in the x direction and s_y the width of the paraboloid in the y direction. The resulting images are shown in Figure 2.5. The reference image is obtained with $\Delta\phi = 0$

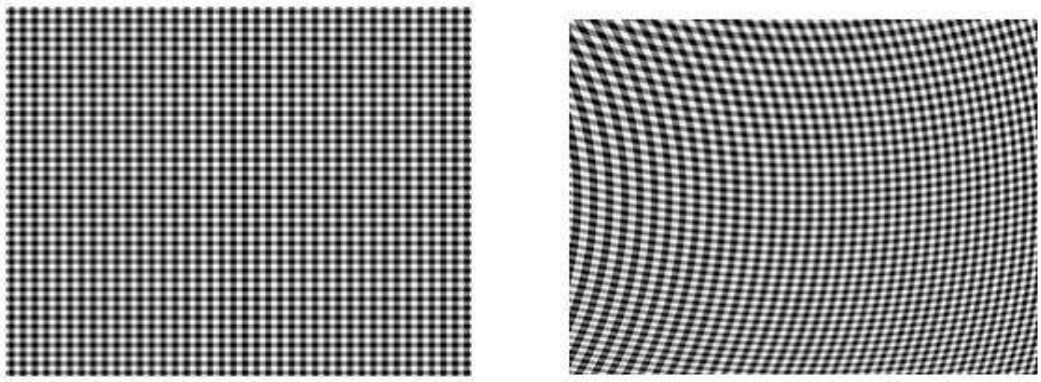

(a) *(b)*

Fig. 2.5. a) Reference pattern of crossed fringes; b) Deformed pattern.

The Fourier method is applied to both images. In Fig. 2.6 we show the Fourier transforms, respectively.

Phase differences corresponding to Figs. 2.6(a) and 2.6(b) are shown in Figures 2.7(a) and 2.7(b) for horizontal and vertical direction respectively. These phase maps are wrapped. Retrieved phases in both directions of the image look the same, so we compare them with the modulating phases originally introduced, by Eq. (2.22) to calculate the accuracy of this method.

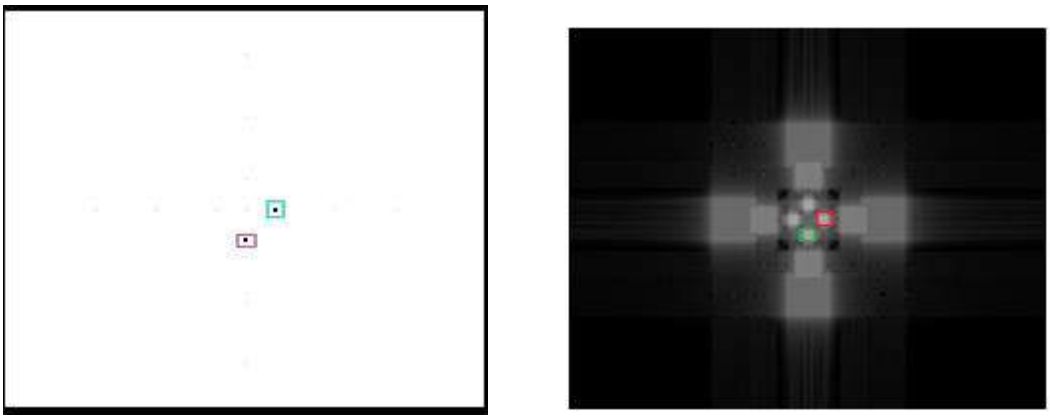

(a) (b)

Fig. 2.6. a) Fourier transform for the reference image (Colors were inverted in order to have a better resolution and distinguish where the lobes are); b) Fourier Transform for the distorted image. The band pass filter used for the lobes in the horizontal direction are shown with the red rectangle in (b), while in green for the vertical direction.

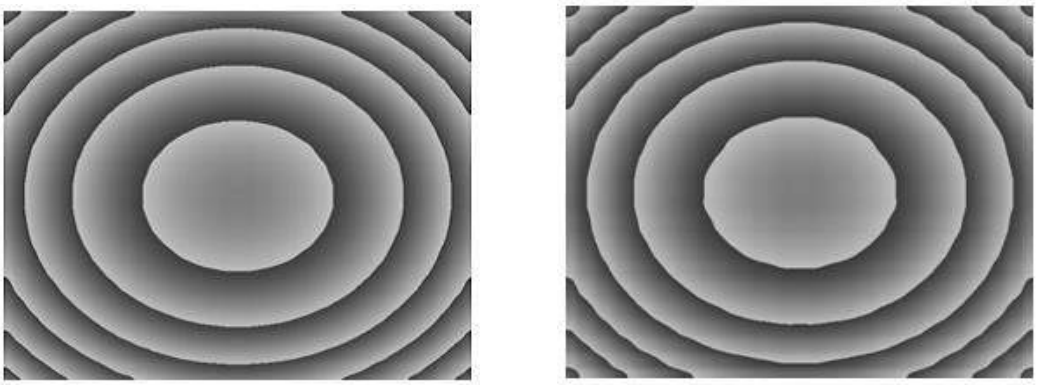

(a) (b)

Fig. 2.7. Wrapped phase maps. a) Horizontal direction; b) vertical direction.

In Fig. 2.8 we show a cross-section of the given and the recovered phase maps.

The result of applying the phase unwrapping algorithm to the wrapped phase is shown in Fig. 2.9, where again a comparison between given and retrieved values of phase are presented.

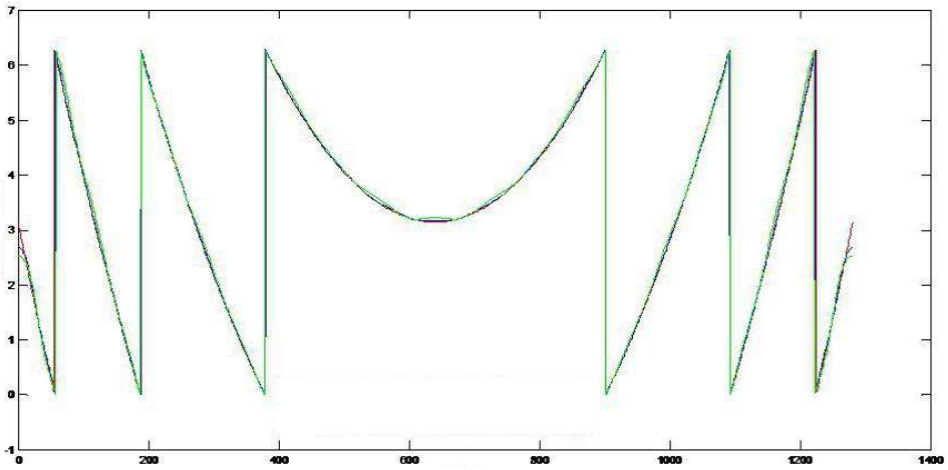

Fig. 2.8. Horizontal cut of the wrapped phases for both directions (blue for horizontal and green for vertical direction) and the modulated phase (red line). Horizontal axis are in pixels and vertical axis are in Radians.

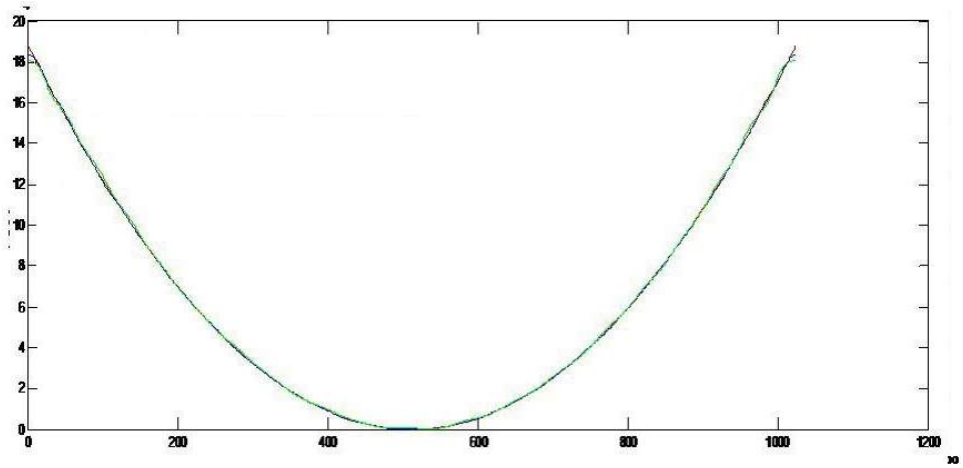

Fig. 2.9. Horizontal cross-section of the unwrapped phases for both directions (blue for horizontal and green for vertical direction) and the modulated phase (red line). Horizontal axis is in pixels and vertical axis is in Radians.

To calculate the error use the following equation,

$$\sigma_t = \sqrt{\frac{\sum_{m=1}^{M}\sum_{n=1}^{N}\left(\Delta\phi_{teor_{m,n}} - \Delta\phi_{obt_{m,n}}\right)^2}{MN}}. \tag{2.23}$$

Based on Eq. (2.23), for the horizontal direction x, the error is found $0.065rad$, which corresponds to a percentage error $of 0.17\%$, whereas for the vertical direction it is $0.12rad$ (0.33%).

As can be seen, the errors regarding the recovery phases are caused by the unwrapping algorithm used but still maintain high accuracy and certainty in the results.

In an experimental situation, once the phases for both spatial directions were calculated, the displacements underwent by the fringes can be calculated by Eq. (2.21), and then we can obtain the gradients of refractive index for both spatial directions via Eqs. (2.6) and (2.7). As a final step, temperature changes can be computed by Eq. (2.8).

Conclusions

This chapter describes the mathematical analysis of the optical techniques used in this work.

As for the processing time requirements, the two techniques are similar. In BOS relatively complex correlation techniques are compared to the complex phase unwrapping algorithms generally used in FD.

BOS and FD are based on the calculation of the derivative of the refractive index. Furthermore these derivatives are available simultaneously along two directions perpendicular to each other.

Once the refractive index is obtained, the distribution of temperature change between two states can be calculated by Eq. (2.8).

Bibliography

[1] J. M. Pinto López, “Medición Interferométrica de Temperatura de una Llama Axisimétrica", Tesis de Maestría en Ciencias de la Ingeniería, Santiago de Chile, Julio, (2007).

[2] S. Doric, “Ray tracing through gradient-index media: recent improvements", Appl. Opt. 29 4026-9 (1990).

[3] J. Hazewinkel, L. R. M. Maas, and S. B. Dalziel, “Tomographic reconstruction of internal wave patterns in a paraboloid,” Exp. Fluids 50, 247-258 (2011).

[4] H. Schardin, “Toepler’s schlieren method, basic principles for its use and quantitative evaluation,” in Selected Papers on Schlieren Optics, SPIE Milestones Series Vol. MS61, SPIE Bellingham, WA. (1992).

[5] W. Hauf and U. Grugull, Optical methods in heat transfer, Academic Press Inc., New York, 166-167 (1970).

[6] O. S. Jensen, J. P. Kunsch, and T. Rosgen, “Optical density and velocity measurements in cryogenic gas flows,” Exp. Fluids 39, 48-55 (2005).

[7] C. Alvarez-Herrera, D. Moreno-Hernandez, and B. Barrientos, “Temperature measurement of an axisymmetric flame by using a schlieren system,” J. Opt. A: Pure Appl. Opt., 10, 104014, 7 pp (2008).

[8] C. Alvarez-Herrera, D. Moreno, B. Barrientos and J. A. Guerrero-Viramontes, “Temperature measurement of air convection using a schlieren system,” Opt. Laser Tech. 41, 233-240 (2008).

[9] E. Goldhahn and J. Seume, “The background oriented schlieren technique: sensitivity, accuracy, resolution and application to a three-dimensional density field,” Exp. Fluids 43, 241-249 (2007).

[10] M. Takeda, H. Ina, and S. Kobayashi, “Fourier-transform method of fringe-pattern analysis for computer-based topography and interferometry,” JOSA A72 (1), 156-160 (1982).

[11] Shakher, C., Nirala, A. K., Pramila, J. and Verma, S. K., “Use of speckle technique for temperature measurement in gaseous flame", J. Optics 23(2): 35-39 (1992).

[12] J. Sznitma and T. Rosgen, “Whole-field visualization and Abel reconstruction of axisymmetric vortex rings,” J. Flow Visual. Im. Proc. 13, 343-358 (2006).

[13] M. Raffel, C. Willert and J. Kompenhans, Particle image velocimetry, a practical guide, Springer-Verlag, Berlin (1998).

[14] D. J. Chen, F. P. Chiang, Y. S. Tan, and H. S. Don, “Digital speckle-displacement measurement using a complex spectrum method,” App. Opt. 32, 1839-1849 (1993).

[15] M. Raffel, C. Willert and J. Kompenhans, Particle image velocimetry, a practical guide, Springer-Verlag, Berlin (1998).

[16] D. J. Chen, F. P. Chiang, Y. S. Tan, and H. S. Don, “Digital speckle-displacement measurement using a complex spectrum method,” App. Opt. 32, 1839-1849 (1993).

[17] G. E. A. Meier, “Computerized background-oriented schlieren,” Exp. Fluids 33, 181-187 (2002).

[18] C. D. Perciante and J. A. Ferrari, “Visualization of two-dimensional phase gradients by subtraction of a reference periodic pattern,” App. Opt. 39, 2081-2083 (2000).

[19] K. J. Gasvik, Optical Metrology, 3rd ed. John Wiley and Sons, Sussex (2003).

[20] D. W. Robinson, Interferogram analysis (digital fringe pattern measurements, IOP Publishing Ltd., Philadelphia (1993).

[21] B. Barrientos, M. Cywiak, W. K. Lee, and P. Bryanston-Cross, “Measurement of dynamic deformation using a superimposed grating,” Rev. Mex. Fis. 50, 12-18 (2004).

3

Numerical analysis of BOS and FD

Contents

Previous studies [1] make use of FD and BOS techniques for the development of research on temperature measurement gradients with analysis of the parameters and variables involved.

In this chapter a numerical analysis of the influence of mainly two parameters (blur and spatial resolution) on the accuracy of the results is presented.

For the numerical simulations, a phase object represented by a Gaussian distribution of the change in refraction index is considered. The equation representing this type of object is Eq. (2.9), given in Chapter 2. One example of this phase object is shown in Fig. 2(a). In this case, the next values of the variables are used: $\Delta n_0 = 6.1 \times 10^{-5}$, $L_x = L_y = 10$ cm, $(x_0, y_0) = (0, 0)$, and $r_0 = 0.2L_x$. The Gaussian function for the index of refraction distribution is a first approximation to represent axisymmetric phase objects, such as the gas jet issued by a gas burner. The projected images of the background are discretized using $448 \times 448\, pixels$. Considering these dimensions in pixels, the corresponding maximum displacement of the above example is $2.5\, pixels$ for any of the components of displacement.

3.1 Background oriented schlieren

As an example for BOS, a case where the maximum of displacement is $7.5\, pixels$ was considered for both Δx and Δy; the associated displacement fields, for each displacement component, are shown in Figs. 3.1(a) and 3.1(b), respectively. Eqs. (2.6) and (2.7) generate the x- and y-components of displacement, respectively (these displacements are denoted as the "given" displacements).

The reference BOS image is composed of 16000 computer-generated Gaussian particles, whose coordinate centers are randomly selected. To generate the displaced image, the center coordinates of the particles is obtained by adding the particle displacement $(\Delta x, \Delta y)$ to the corresponding reference center coordinates. The displaced image is shown in Fig. 3.1(c). This image and the reference image are then used to calculate the related displacement fields by using the Fourier algorithm given by Eq. (2.10).

Performance of BOS may be obtained by comparing the given displacements with the values computed via the Fourier correlation algorithm. The correlation calculation is obtained by Particle Image Velocimetry (PIV) software from IDT (Provision-XS). [2] The corresponding displacement calculations are shown in Figs. 3.1(e) and 3.1(f), for the x- and y-components, respectively. Furthermore, in Figs. 3.1(g) and 3.1(h), cross sections of the two components of displacement, for row 10 and column 143, are shown, respectively; each figure contains four plots: the given displacement values are shown by solid line (subscript g) and the computed or recovered values by discontinuous line (subscript c). Displacements are given in pixels. The particle radius was selected to be either one or two pixels; as shown below, these values yield optimal results. For evaluation purposes of FD and BOS, it is not necessary to compare the given and the computed fields of the change in refraction index, but only the displacement fields.

The rms error for the numerical results is calculated by taking into account the given displacements $(\Delta x_g, \Delta y_g)$ and the computed values $(\Delta x_c, \Delta y_c)$. The error in the calculation of the x-component of displacement can be expressed as

$$e_x = \sqrt{\frac{\sum_{i=1}^{N} \left(\Delta x_{i,c} - \Delta x_{i,g}\right)^2}{N}}, \tag{3.1}$$

where N is the total number of displacement vectors. For the error in the y-displacements, a similar expression to Eq. (3.1) can be used. The corresponding relative errors can be found by dividing Eq. (3.1) by$\max(\Delta x_g)$, where $\max()$ denotes a function that gets the maximum value of the argument. Additionally, the total relative error can be determined as$e = \sqrt{e_x^2 + e_y^2}/\max(\Delta_g)$, where$\Delta_g = \sqrt{\Delta x_g^2 + \Delta y_g^2}$.

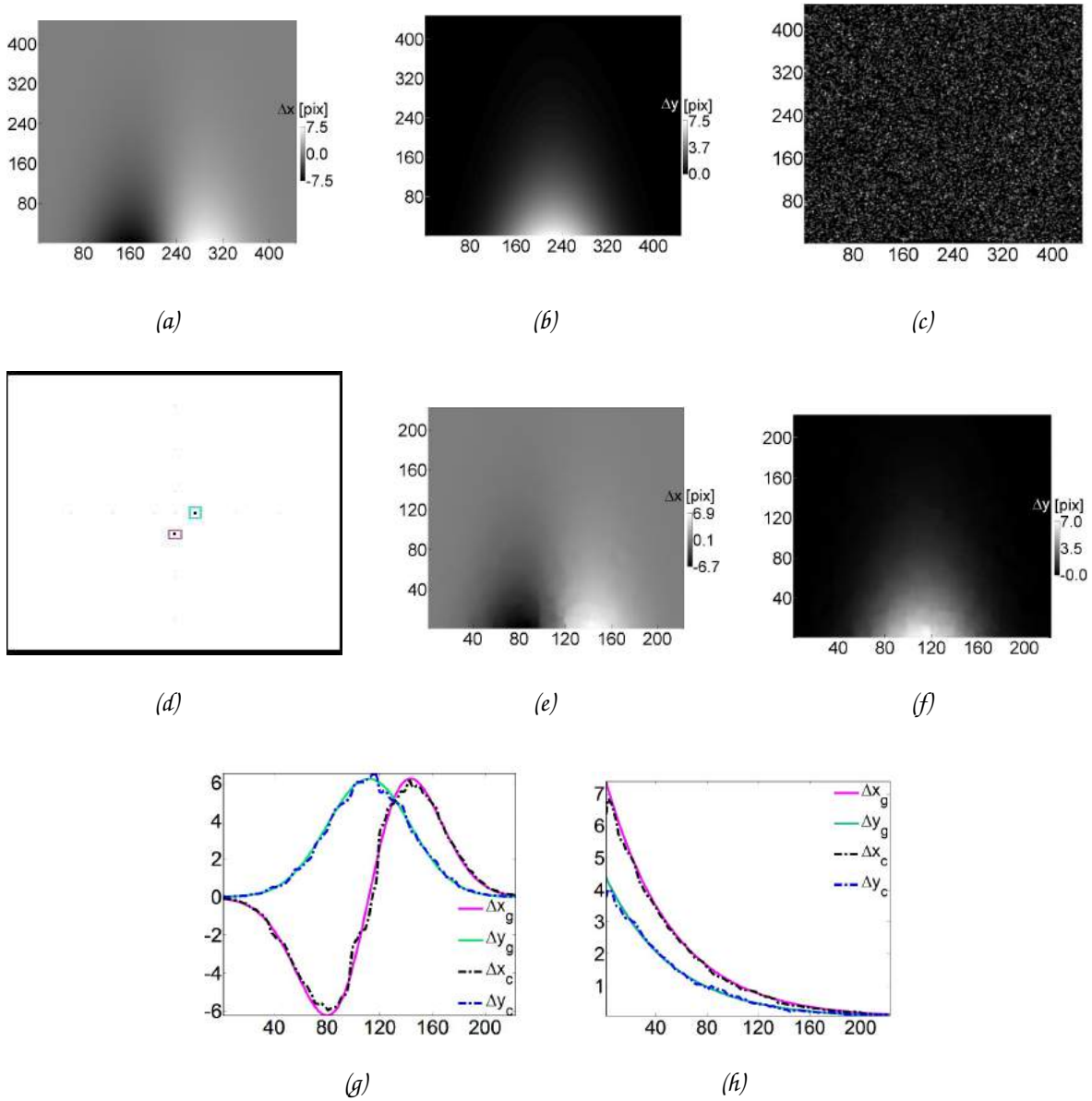

Fig. 3.1. Influence of displacement range on accuracy of BOS. Typical given displacement maps, for (a) x-displacement component, (b) y-displacement component. (c) Displaced image. Corresponding computed displacement distribution, (d) x-displacement component, (e) y-displacement component. Cross sections for (f) row 20, horizontal and vertical components of displacement and (g) column 287, horizontal and vertical components of displacement. In legends, subscripts g and c denote given and computed displacements, respectively. (h) Percentage relative errors, when varying the size of the correlation sub image (in pixels), for several values of the maximum of displacement (0.5, 2.5, 5.0 and 7.5 pixels). Axis are in pixels. Negative values in the vertical axis of part (g) denotes that the zero was set at the center of the image (column 224)

A numerical error analysis is presented to get insight into the performance of the Fourier correlation method; we vary the values of maxima of displacement from $0.5\ pixels$ to $7.5\ pixels$. These values can be selected by changing the maximum variation of the refractive index Δn_0. Furthermore, the size of the correlation sub images is varied as well, where squared sub images of 16×16, $24x \times 24$, 32×32, 64×64 and $128 \times 128\ pixels$ are assumed. Figure 3.1(h) shows plots containing the resulting percentage relative errors of this analysis (an object-to-background distance D of $6\ m$ is selected). By applying an interpolation technique to the correlation results, it is possible to increase the number of resulting vectors for each image (in this case, $224x224 = 50167$ vectors are used).

We have found that the best results are obtained for correlation window sizes of $16 \times 16\ pixels$ and $32 \times 32\ pixels$. In general, low accuracy is obtained for a sub image size of $128 \times 128\ pixels$. This is due to the relatively large gradients of the displacement field that are implicit in the analysis. In connection with the maximum displacement, values in the range $2.5 - 5.0\ pix$ are seen to optimize the calculation, resulting in relative errors around 0.5%.

3.2 Fringe Deflection

In order to have displacement sensitivity in two mutually perpendicular directions, two crossed gratings are used. The reference square grating may be expressed as,

$$I_1(x,y) = a(x,y) + b_x(x,y)\cos(2\pi f_{0,x}x + \phi_{ref,x}) + b_y(x,y)\cos(2\pi f_{0,y}y + \phi_{ref,y}), \quad (3.2)$$

Where subscripts x and y denote the direction of the intensity variation (which is perpendicular to the orientation of the grating). An example of an intensity image obtained by this equation is shown in Fig. 3.2(a) for a grating period of $14\ pixels$.

Likewise, the displaced image may be given by

$$I_2(x,y) = a(x,y) + b_x(x,y)\cos\left[2\pi f_{0,x}(x-\Delta x) + \phi_{ref,x}\right] + b_y(x,y)\cos\left[2\pi f_{0,y}(y-\Delta y) + \phi_{ref,y}\right]; \quad (3.3)$$

and for the phase object of the previous section –considering the displacement fields shown in Figs. 3.1(a) and 3.1(b)–, the resulting image is shown in Fig. 3.2(b).

Application of the Fourier method to the reference and the displaced images, implies the calculation of the Fourier transforms of images in Figs. 3.2(a) and 3.2(b). Figure 3.2(c) contains the corresponding result for the displaced image. In this figure, we also show the band-pass filters applied to the horizontal and vertical side lobes (related to the vertical and horizontal gratings, respectively), and they are indicated by the dashed rectangles. The filters are not applied simultaneously. As it is observed, the size of the filters is selected in such a way that the number of frequency components, related to a side lobe, that are allowed to pass, is maximized. This type of selection minimizes any averaging effect that may affect the calculations.

After filtering the Fourier-transformed images, four images are generated: two images for the reference state related to each one of the two filters, and, analogously, two more images for the displaced image. The inverse Fourier transform of the four images was then taken. The relative phase related to the x-component displacement can be recovered directly from the Fourier map produced by the filter indicated by the larger dashed rectangle (associated with the vertical grating) as [3], [4]

$$\Delta\phi_x\left(x,y\right) = 2\pi f_{0,x}\Delta x(x,y) = \tan^{-1}\left(\frac{S_{1x}C_{2x} - S_{2x}C_{1x}}{S_{1x}S_{2x} + C_{1x}C_{2x}}\right), \tag{3.4}$$

Where S_i and C_i are defined as in Eq. (2.20); for example $C_{1x} = \frac{1}{2}b_x(x,y)\cos(2\pi f_{0,x}x + \phi_{ref,x})$ and $S_{2x} = \frac{1}{2}b_x(x,y)\sin\left[2\pi f_{0,x}(x-\Delta x) + \phi_{ref,x}\right]$. Here $i = 1, 2$ designates the reference and the displaced images, respectively.

Similarly, the recovered phase related to the y-component of displacement becomes (by using the smaller filter, which is associated with the horizontal fringes)

$$\Delta\phi_y\left(x,y\right) = 2\pi f_{0,y}\Delta y(x,y) = \tan^{-1}\left(\frac{S_{1y}C_{2y} - S_{2y}C_{1y}}{S_{1y}S_{2y} + C_{1y}C_{2y}}\right). \tag{3.5}$$

Phase maps calculated by Eqs. (3.4) or (3.5) may give rise to wrapped phase maps when the absolute phase values are larger than π rad. When this occurs, an unwrapping algorithm [5] may be applied. As indicated by the first equalities of Eqs. (3.4) and (3.5), phase and displacement are proportional.

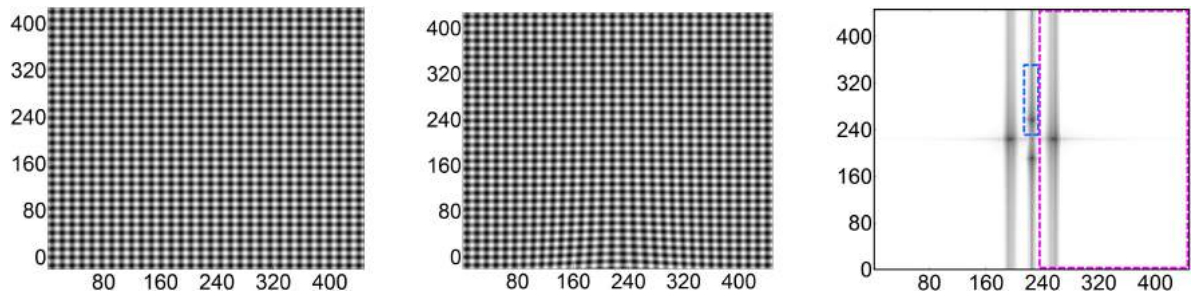

Fig. 3.2. A typical pair of FD images, (a) reference and (b) displaced. (c) Fourier transform of (b); band-pass filters for vertical and horizontal gratings are indicated by dashed line (right half-plane and smaller rectangle, respectively). The cross gratings have a period of $14\ pixels$*. The value for the maximum displacement is* $7.5\ pixels$*, for both directions. Axis are in pixels.*

For the current example, the maps related to the calculated components of displacement, horizontal and vertical, are shown in Figs. 3.3(a) and 3.3(b), respectively. Further, in Fig. 3.3(c), cross sections of Figs. 3.3(a) and 3.3(b) are showed, along the horizontal direction for row 20. They are indicated by discontinuous line. The results obtained by the horizontal grating, subscript H, are shown by thicker discontinuous line. Similarly, in Fig. 3.3(d), cross sections of Figs. 3.3(a) and 3.3(b) in the vertical direction are shown, column 287. The solid curves in Figs. 3.3(c) and 3.3(d) are related to the corresponding given displacements. The thinner solid lines represent the component of displacement related to the vertical grating, subscript V. Note that the dashed curves (recovered values) coincide with the continuous curves (given values) for almost all points. In addition, a relatively large discrepancy is observed at the edges of the curves of the displacement associated with the horizontal grating (for the cross sections) along the vertical direction. This is due to aliasing effects stemming from the non-periodicity of the spatial object along the y-direction. This effect may be reduced as it has been shown in the literature. [5], [6]. Evaluation of FD can be realized by the computation of the rms error via Eq. (3.1). The rms relative error for the present case is 0.015%.

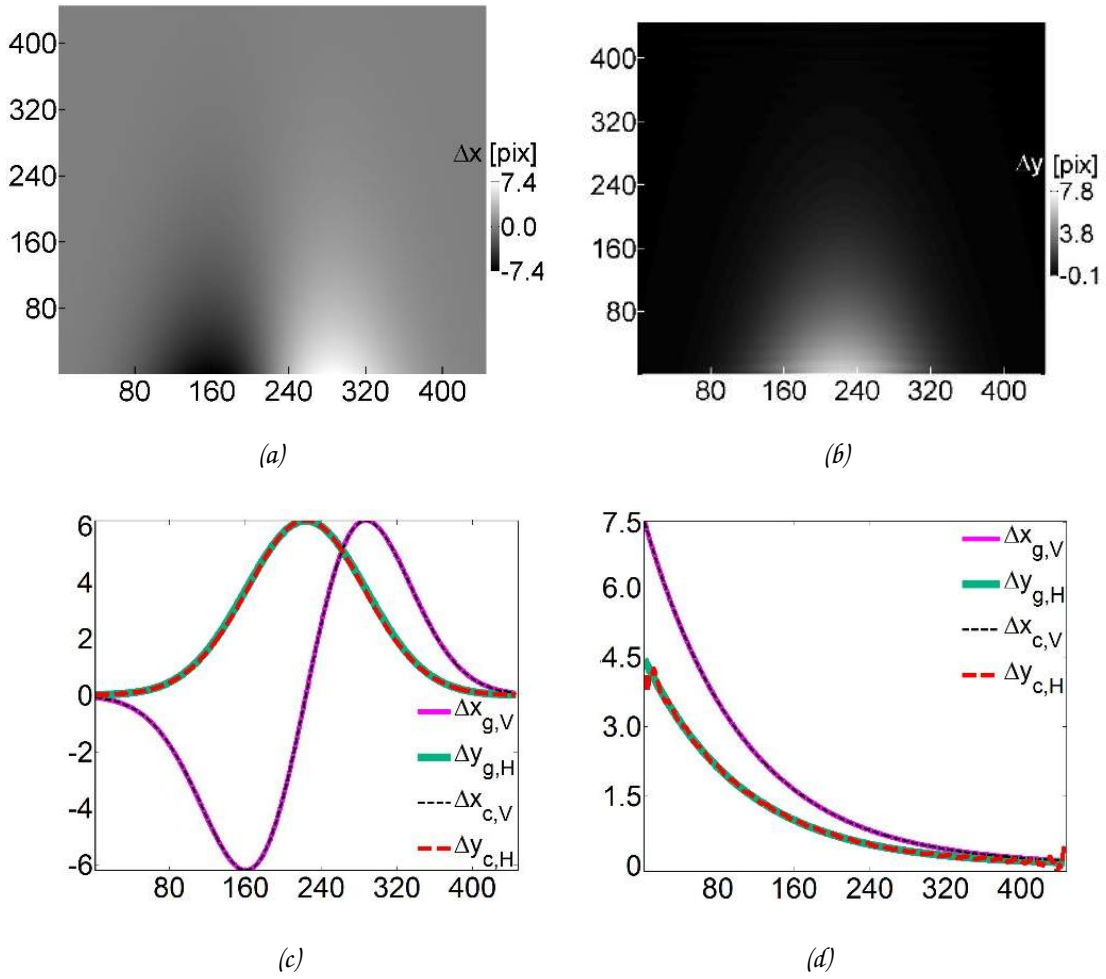

Fig. 3.3. An example of computed displacement maps arising from: (a) Vertical grating (related to x-displacements) and (b) horizontal grating (related to y-displacements). Image size is $448 \times 448\ pixels$*. Cross-sections of the two previous maps and of the given displacement maps (not shown), along: (c) x-direction –row 20– and (d) y-direction (column 287). Dimensions for axes are pixels.*

Next, for FD, an analysis similar to that carried out for BOS in Sec. 3.1 was done, where the maximum of displacement was varied. Results of percentage relative errors are shown in Fig. 3.4, where in 3.4(a) and 3.4(b), the profile of the fringes is assumed sinusoidal, as in Eq. (3.2). These two figures show the errors in the relative phase related to the horizontal and vertical gratings, respectively.

Sinusoidal fringes are difficult to attain in practice because each optical component of the setup (projector, imaging lens and sensor) presents non-ideal optical transfer functions. A more realistic profile for

the fringes is that represented by a periodic Gaussian function, which can be modeled by its Fourier series. The results for the error analysis for this type of fringes are shown in Figs. 3.4(c) and 3.4(d), for horizontal and vertical gratings, respectively. On all graphs in Fig. 3.4, the values of the y-axis should be scale down by 10^{-3}. The horizontal axis represents the period of the crossed gratings, which takes on the values of 3, 5, 7, 10, and $14\ pixels$. Each figure contains four plots; they correspond to different values of the maximum of displacement, 0.5, 2.5, 5.0 and $7.5\ pixels$.

As it is noticed from the plots, the percentage relative error obtained for horizontal fringes is greater than for vertical fringes. This is due to aliasing effects, as mentioned above. When the grating period is a multiple of the size of the image, aliasing effects are reduced [7], and larger values of accuracy are obtained.

In general, for a given period, relatively large displacements imply large errors [8]. In the case of Gaussian fringes, the discrepancy increases for relatively small and large grating periods.

Overall, the accuracy of the Gaussian fringes is lower than for sinusoidal fringes. However, even in this case, the resulting accuracy of FD is greater than that obtained by BOS.

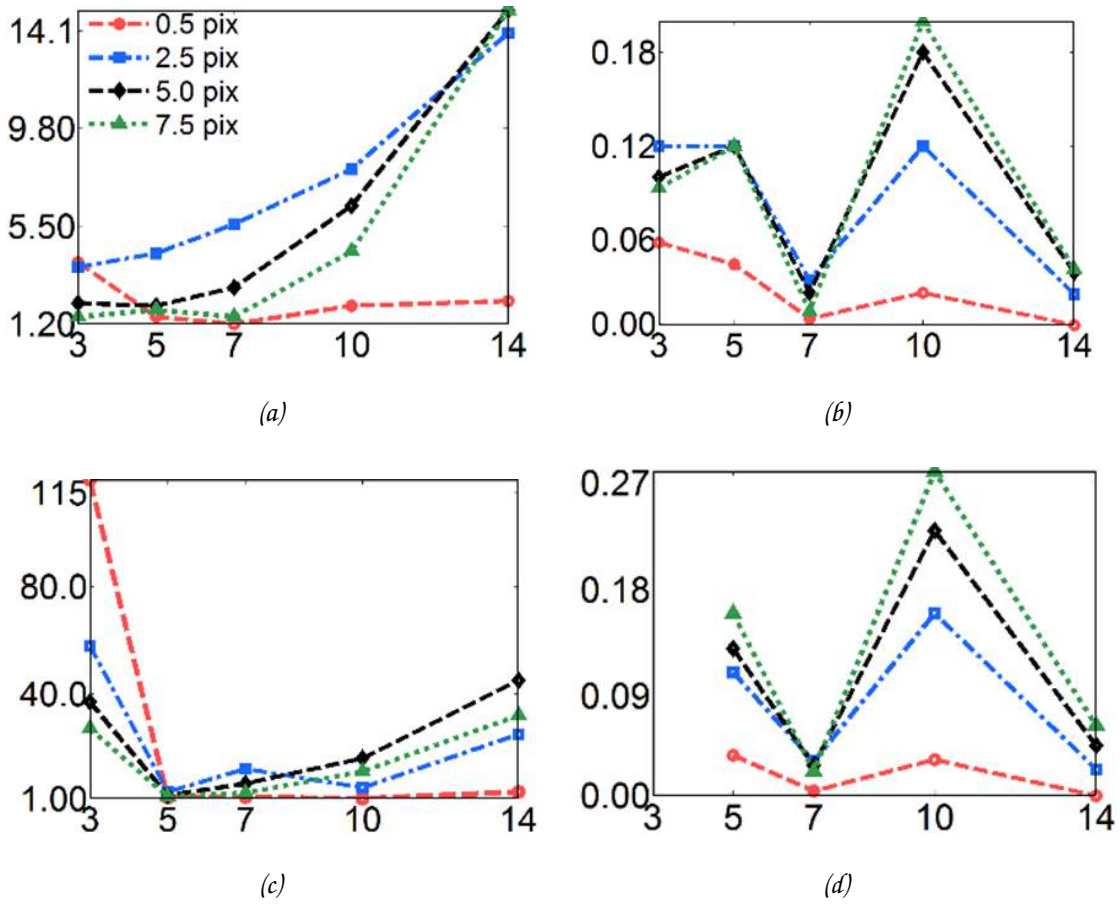

Fig. 3.4. Percentage relative errors (vertical axis) vs period (horizontal axis) in pixels for FD (displayed values of errors should be multiplied by 10^{-3}), with m, for different values of the maximum of displacement, calculated for sinusoidal fringes using: (a) horizontal grating and (b) vertical grating; and for Gaussian fringes using: (c) horizontal grating and (d) vertical grating. Information for 3 pixels in (d) is not shown because of scaling reasons, but it is similar to the corresponding in (c).

3.3 Relationship between temperature and displacement

Since the range of values of the displacements influences the accuracy of BOS and FD, an analysis of the relationship of this parameter and the temperature is given next. First, take a Gaussian variation of the refractive index, as that expressed by Eq. (2.9).

The maximum $x - component$ of displacement is attained at $x = r_0/\sqrt{2}$. By using $x_0 = 0$ and $y = 0$, Eq. (2.10) yields the maximum displacement $\Delta x_{MAX} = 1.5D\Delta n_0/n_0$; hence, by solving Eq. (2.8) for n, we find that

$$\Delta x_{MAX} = -\frac{1.5D}{n_0}\left(\frac{T_0}{T} - 1\right)(n_0 - 1)\,. \tag{3.6}$$

In Fig. 3.5, relationship (3.6) for a range of temperatures of $2000\,^oC$ was plotted. Each plot represents a different value of object-to-background distance D; for a typical D of $6\ m$, the maximum displacement is less than $7\ pixels$. Considering the results of the last two sections, both FD and BOS can adequately handle this value of displacement.

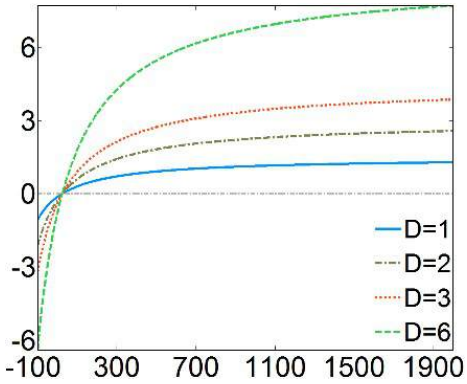

Fig. 3.5. Relationship between maximum of displacement (in pixels, vertical axis) and temperature (in ^oC, abscissa) for varying object-to-background distance D (1, 2, 3 and $6\ m$). Reference values for temperature and index of refraction are $T_0 = 25\,^oC$ and $n_0 = 1.00022$.

3.4 Evaluation of spatial resolution

Unlike FD, where the number of displacement vectors equals the number of pixels of the images, BOS yields a number of vectors that depends on the size of the correlation sub images and the level of interpolation. Then, it may be expected that the spatial resolution of FD be larger than that of BOS. To show this, a numerical phase object is constructed so that the distribution of the change in refractive index contains a narrow depression. In practical terms, this depression may represent a lower temperature region that under certain conditions appears at the exit of gas nozzles. This situation can be modeled as the difference of two Gaussian functions, each function with different diameter and amplitude.

For example, in Figs. 3.6(a) and 3.6(b), the resulting displacement components for a subtracting Gaussian function with a diameter of $1/10$ the diameter of the main Gaussian function is showed. A maximum displacement of $2.5\ pixels$ is assumed for both horizontal and vertical displacement components. The subtracting Gaussian function is located at the center of the observation region and its amplitude is 80% of the amplitude of the main function. Cross sections of the associated map of the change in refractive index (not shown) are illustrated in Fig. 3.6(c), for three different amplitudes of the subtracting Gaussian: 0.2, 0.4 and 0.8, referenced to the amplitude of the main Gaussian function (amplitude of 1.0). The cross sections are along row 10.

By analyzing the diameter and the amplitude of the subtracting Gaussian function, influence of spatial resolution on accuracy can be modeled.

In Figure 3.7, results of the analysis for FD and BOS are shown. By considering the given values of the distribution of the refractive index, as those shown in Fig. 3.6(c), corresponding values of displacement can be found. In Fig. 3.7(a), cross sections of the maps of the horizontal component of displacement, shown in Fig. 3.6(a), along row 10 are showed. Two cases for different amplitude of the subtracting Gaussian function are included.

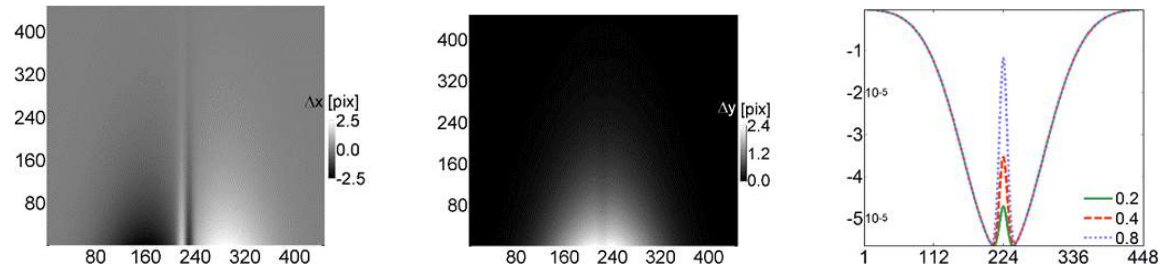

(a) *(b)* *(c)*

Fig. 3.6. A flame distribution with a low-temperature zone at its center. Displacement maps for (a) the x-component of displacement and (b) the y-component. (c) Horizontal cross section, row 10, of the change in index refraction for a subtracting Gaussian function of radius of $1/10$ *of the diameter of the main function and for three values of amplitude,* 0.2*,* 0.4 *and* 0.8*. In parts (a) and (b) axis are in pixels. Part (c) vertical axis has no units and has an order of* 10^{-5}

In Figures 3.7(b) to 3.7(d), FD results are presented for the $x - component$ of displacement –they are indicated by lines with markers. For comparison reasons, curves of the given values are also included and are shown by lines without markers. The ordinate axes refer to displacement in pixels.

Each figure from (b) to (d) corresponds to a different value of the diameter of the subtracting Gaussian; three different values are considered, $1/10$, $1/20$ and $1/30$ of the diameter of the main Gaussian function. The plots in each figure represent different values of the amplitude of the subtracting Gaussian (0.2, 0.4 and 0.8). For clarity reasons, we show only the central zone of the region under analysis, where the subtracting Gaussian function is located. It is observed that the smaller the diameter of the depression, Fig. 3.7(d), or the larger the amplitude of the subtracting Gaussian function– indicated by the dotted line plots–, the bigger the discrepancy between the given and the computed displacement fields. For this analysis, a grating period of $3\ pixels$ is assumed.

A similar analysis is done for BOS, and the results are presented in Figs. 3.7(e) - 3.7(g). As it can be noticed, the same behavior is found as in FD, but discrepancies between the given and computed values are larger. Figure 3.7(g), which is related to the smaller diameter of the depression, shows that the depression is not resolved for any of the three cases of amplitude of the subtracting Gaussian function.

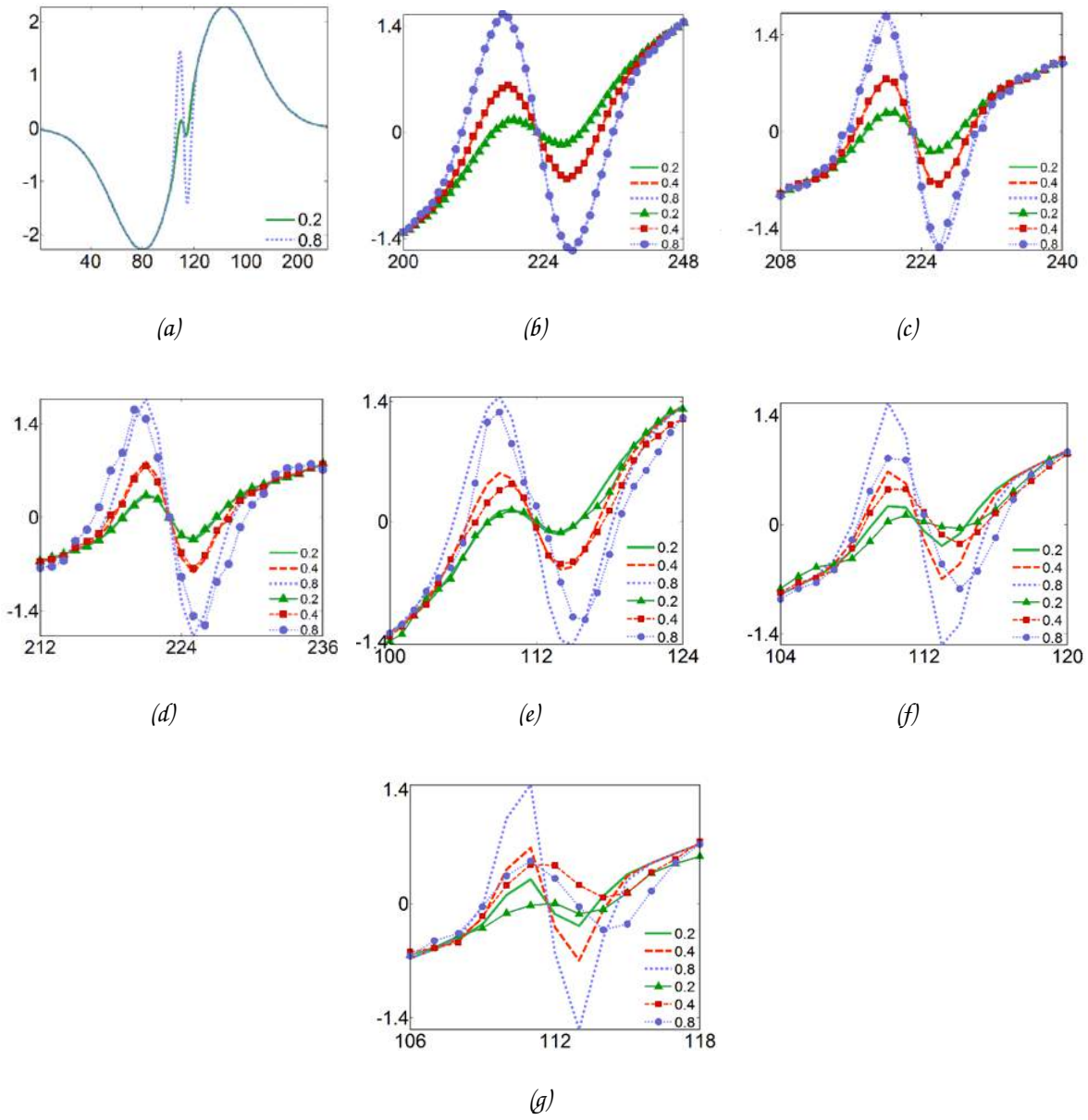

Fig. 3.7. Cross sections, along row 10, of the horizontal component of displacement. (a) Given displacement values for a diameter of the subtracting Gaussian function of $1/10$ *that of the main Gaussian function. Two different cases of the amplitude of the subtracting Gaussian function are included, where* 1.0 *is the amplitude of the main Gaussian function. For FD results: (b)-(d) correspond to different diameters of the subtracting Gaussian function,* $1/10, 1/20$ *and* $1/30$ *of* r_0 *, respectively. Each figure contains three cases of different amplitude of the subtracting function,* $0.2, 0.4$ *and* 0.8*. The curves representing the given data are indicated by lines without markers and the computed curves by lines with markers. For BOS, (e)-(g) are read in a similar way as those for FD. Axes are in pixels. Negative values in the vertical axis are because the zero pixel was set at the center of the image.*

3.5 Evaluation of robustness

Blurred regions may appear in recorded images either when changes of the phase object take place in times shorter than the exposure time of the camera, or when the object is not in focus. Next, it was evaluated FD and BOS when the recorded images contain regions with low levels of contrast. To simulate this issue, an averaging filter of $7\ pixels$ in width is applied to the central region of the intensity images. The strength of the filter is varied gradually from 0, at the edges of the blurred region, to 1, at the center of the region. As in the previous section, a maximum value of $2.5\ pixels$ for each displacement component is assumed.

A typical blurred FD image is shown in Fig. 3.8(a), where the averaging filter is applied twice. By varying the number of times that the filter is applied, the degree of blurring could be selected. In Fig. 3.8(b), horizontal cross sections were presented, row 20, of the calculated x-component of displacement; here five plots that represent the number of times that the averaging filter is applied (blurring level) are showed, 0-4 times, where the 0-case corresponds to no blurring (indicated by continuous line without markers). The cases with blurring are indicated by either discontinuous line or by lines with markers.

An analogous numerical simulation for BOS is presented in Figs. 3.8(c) and 3.8(d). FD is slightly more robust than BOS as it can seen, and that for regions with large levels of blur (where the averaging filter is applied four times), both methods produce incorrect results. It is important to note that for FD, the period of the fringe pattern used for obtaining these results is $12\ pixels$. With this relatively large period, despite the fact that the error gets large, according to Fig. 3.4, FD can tolerate more blurring than BOS, as long as the size of the averaging filter is less than half the grating period.

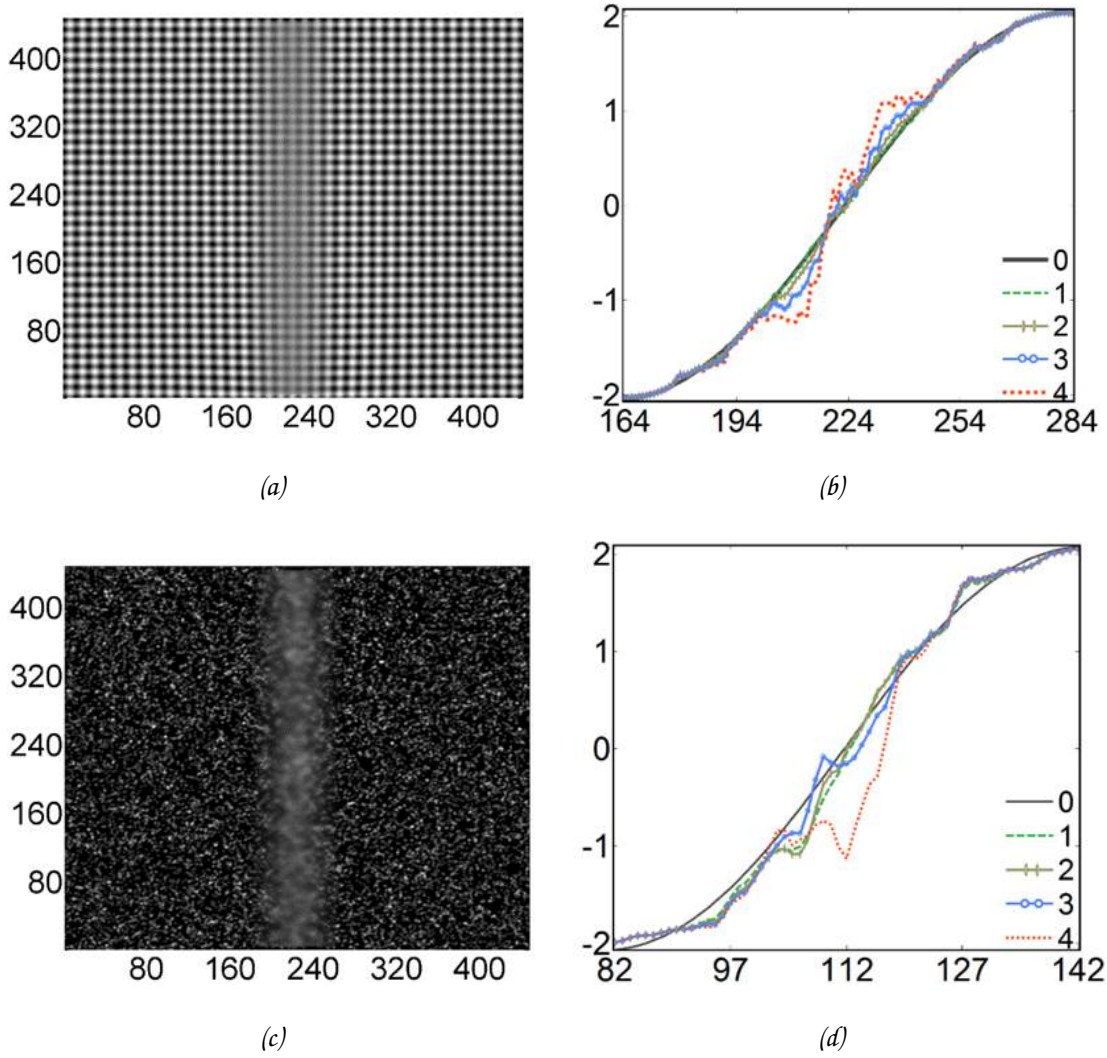

Fig. 3.8. Evaluation of level of contrast. For FD, (a) typical blurred image (averaging filter is applied 2 times), (b) Horizontal cross-sections, row 20, of the horizontal component of displacement. The number of times the filter is applied is varied from 0 to 4. Only the central zone is shown. For BOS, (c) and (d) are described as those for FD. Axes are in pixels. Negative values in the vertical axis are because the zero pixel was set at the center of the image.

The procedure to generate all the analysis is described below.

1. Generate the image with particles, which are located randomly. The profile of the particles is Gaussian, according to Eq. (2.9). In this way the reference image is created, $I\left(x,y\right)$.

2. Generate the distribution of displacements for each particle. The displacements $(\Delta x, \Delta y)$ take the given values by Eqs. (2.10) and (2.11).

3. Produce the displaced image $I\left(x+\Delta x, y+\Delta y\right)$ by assigning the latter displacements to each particle of the reference image.

4. Correlate the reference and displaced images by using either correlation by Fourier Transform and the Fourier phase method. This yields the recovered displacements.

5. Calculate the percentage relative errors by using the recovered and given values of the displacement.

3.6 Conclusions

The performance of BOS and FD was evaluated by means of numerical simulations. For Gaussian distributions of refractive index, the accuracy for FD, for typical associated displacements, was larger than that obtained by BOS was founded out. For relatively small and large displacements ($0.5\ pixels$ and $7.5\ pixels$, respectively) of the spatial structures of the background, errors tended to be rather large for both techniques.

Fringe deflection requires less numerical processing and its programming code is simpler when compared to BOS, especially when care is taken so that the maximum displacement is smaller than the period of the gratings, avoiding the use of any unwrapping algorithm. Besides, as FD can yield the desire physical variable at all pixels of the images, its spatial resolution is slightly larger as well; in BOS, the spatial resolution is limited by the size of the sub-window.

The numerical results also showed that FD tolerates slightly larger levels of blurring of the images. A weakness of FD arises when images are not periodical in x- or y-directions. However, even under this condition, for the particular object phase we dealt with, it is apparent that FD slightly outperforms BOS.

Bibliography

[1] A. Blanco, “Comparación de Tres Métodos Ópticos para la Medición de Temperatura en Objetos de Fase”, Tesis de Maestría en Ciencias (Óptica), Centro de Investigaciones en Óptica A.C., León, Gto., Enero (2011).

[2] ProVISION-XS PIV 3.12.01, 2014, by IDT, FL. USA. Available from http://www.idtvision.com/high-speed-cameras/products/software/provision/.

[3] . K. Qian, S. H. Seah, and A. K. Asundi, “Algorithm for directly retrieving the phase difference: a generalization,” Opt. Eng. 42, 1721-1724 (2003).

[4] T. Kreis, “Digital holographic interference-phase measurement using the Fourier-transform method,” JOSA A 6, 847-855 (1986).

[5] . K. J. Gasvik, Optical Metrology, 3rd ed. John Wiley and Sons, Sussex (2003).

[6] . S. Vanlanduit, J. Vanherzeele, P. Guillaume, B. Cauberghe, and P. Verboven, “Fourier fringe processing by use of an interpolated Fourier-transform technique,” App. Opt. 43, 5206-5213 (2004).

[7] J. B. Liu and P. D. Ronney, “Modified Fourier transform method for Interferogram fringe pattern analysis,” App. Opt. 25, 6231-6241 (1997).

[8] A. Blanco, B. Barrientos, and C. Mares, “Comparison of Background Oriented Schlieren and Fringe Deflection in temperature measurement”, SPIE Vol. 8011, 801180; doi:10.1117/12.903403, (2011).

4

Experimental analysis of BOS and FD

Contents

In Chapter 2, we reviewed the theory of Background-Oriented Schlieren (BOS) and Fringe Deflection (FD). In Chapter 3, numerical simulations evaluated the performance of these techniques [1]; a phase object represented by a Gaussian distribution of the change in index of refraction was considered. Displacement maps were obtained by digital correlation in BOS and by a phase technique in FD.

The aim of this Chapter is to evaluate experimentally two features of BOS and FD: The spatial resolution and the sensitivity to image blur [2]. The evaluation is done when the techniques are used for the measurement of gradient of temperature.

The two techniques were implemented separately. Similar experimental conditions are maintained. The object corresponds to an axisymmetric flame issued by a gas burner. Displacement maps are measured and the results are compared. For a better comparison of BOS and FD, a setup that warrants simultaneity of the measurements through both techniques is employed. In this case, the information needed by BOS and FD is encoded in the RGB signal of a color image [4]- [6]. By displaying this color image on a monitor, it can be recorded by a color camera.

The images corresponding to each color channel of the recorded images are then available for analysis. The proposed color encoding is similar to the one used in Refs. [7] and [8], where the authors used a background image formed by three superimposed patterns of different color. The additional information enabled them to increase the accuracy of BOS.

Results of the evaluation of the spatial resolution are given in next section. This evaluation comprises the analysis of a small depression, which is formed at the exit of the gas nozzle. For this analysis, two different sizes of the region of observation are considered. Fringe deflection and BOS are applied either separately or simultaneously. In Sec. 4.2, the sensitivity of the techniques to blur is reported.

4.1 Experimental evaluation. Spatial resolution

The object under study is a hot jet issued by a gas burner that uses butane gas at $10350\ Pa$. This type of object presents a temperature distribution similar to that assumed in the numerical simulations of Chapter 3. The values of the distances D and d are $70\ cm$ and $430\ cm$, respectively. The imaging lens corresponds to a $70 - 210\ mm$ zoom lens working at an f-number of 16. To register the images, a Lumenera $2/3''$ camera, model Lu165 ($1024 \times 1280\ pixels$), with an exposure time of $30\ ms$ at $15\ fps$ was used. Additionally, a color Litemax monitor, model SLD1968 (resolution of $1024 \times 1280\ pixels$ and brightness of $1600\ cd/m^2$), is used for displaying the background patterns.

The spatial resolution of BOS and FD is analyzed by reviewing a small depression that is formed at the exit of the burner. The depression comprises an inner region of the jet, which shows relatively low values of temperature. Additionally, two different sizes of the region of observation were reported: $11 \times 21\ cm^2$ and $5.5 \times 10.5\ cm^2$.

The periodic structure of the monitor may give rise to moiré effect when displaying the gratings employed by FD. We avoid this effect by selecting the grating periods of the background image so that they correspond to a multiple of the period of the monitor. Moreover, for BOS, a synthetic background image composed of 40000 computer-generated Gaussian particles of an average radius of $2\ pixels$ (with respect to the resolution of the monitor) is used. At the image plane, the average particle diameter is around $4\ pixels$, considering the larger region of observation.

High contrast of the spatial structures of the background is obtained in a similar way than with printed structures; the principal parameters influencing the contrast are the diameter of the lens aperture, the exposure time and the spatial resolution of the monitor, the sensor and the lens. Considering the spatial resolution of the monitor, when the average size of the structures is larger than two pixels –of the monitor–, images with enough contrast are obtained. A similar condition is observed for the resolution of the combi-

nation lens-sensor. In connection with the diameter of the aperture, this parameter is set to its minimum value in order to image both the object and the background. Then, a correct value of the contrast can be attained by selecting a relatively large value of the exposure time. The exposure time, in turn, must be short enough to capture the desired temporal scale of the dynamic event under study.

The x- and y-axes are perpendicular between them and are located in the plane of the background, as observed in Fig. 2.1. The z-axis, which is along the optical axis, is perpendicular to the background plane. The horizontal and the vertical directions are associated with the x- and y-axes, respectively. Accordingly, in the reported figures, the predominant direction of the convection jet is along the x-axis.

4.1.1 Large region of observation

The images for FD and BOS are firstly registered sequentially; i.e., two consecutive sets of images of the object are recorded, one with the BOS background image and the other with the FD background. General experimental conditions are assumed to remain unchanged during the recording of the two sets of images. This condition is fulfilled only in the region of the gas jet that is close to the exit of the nozzle; other regions of the jet are largely affected by turbulence effects. However, the region that enables to have had some insight of the spatial resolution is precisely the region at the exit of the nozzle, where a temperature depression is formed.

When implementing the techniques, first, a reference image without phase object is recorded. Then, after introducing the object, a series of displaced images are registered. These images are then compared with the reference image in order to retrieve the corresponding displacement maps.

In Fig. 4.1(a), a typical raw image of the FD background pattern, which consists of a set of crossed fringes of periods $4.9\ pixels$ and $9.9\ pixels$, along the horizontal and vertical directions, respectively is showed. The size of the raw images is $710 \times 1280\ pixels$. For clarity reasons, only sections of the

obtained displacement maps are shown in the figures below.

By comparing FD images, with and without the hot gas jet, maps corresponding to the two components of displacement (Δx, Δy) are obtained, as shown in Figs. 4.1(b) and 4.1(c), respectively. In obtaining the associated phase maps by means of the Fourier method, a rectangular band-pass filter of $60 \times 60\ pixels$ is applied in the Fourier domain. Similar results for BOS are presented in Figs. 4.1(d) - 4.1(f). In this case, the displacement maps are calculated via digital correlation, by using Fourier transformations. A correlation sub-window of $8 \times 32\ pixels$ is used, and $256 \times 256\ vectors$ are produced. The commercial software Provision-XS by IDT19 calculates the correlation maps. Both FD and BOS are capable of yielding the two in-plane components of displacement.

In order to compare the results from FD and BOS, the BOS maps are interpolated to produce maps of $710 \times 1280\ pixels$. Corresponding vertical cross sections of the Δy maps for both techniques are shown in Figs. 4.1(g) - 4.1(i). Each of these figures represents the data of a certain column; one of the columns, column 5, is located at the exit of the jet –at the left side of the figures. Lines with markers show the BOS results.

As observed, the displacement maps are similar up to the first half of the region of observation; beyond this zone, they differ because of turbulence effects. An important point to highlight is the ability of FD to measure relatively large temperature gradients, as those presented at the exit of the jet, where the depression is located. As it is noticed from the cross sections for columns 5 and 21, the two narrow peaks associated with those gradients can be fully detected by FD, but only partially by BOS. This difference has to do mainly with the averaging nature of BOS: when calculating the correlation map, sub-windows with finite size are used. To increase the detection ability of BOS, we can reduce the size of the sub window, but a decrease in the accuracy will be observed, since less spatial information is available for analysis.

We assume that the results with the highest accuracy are the ones obtained for a smaller region,

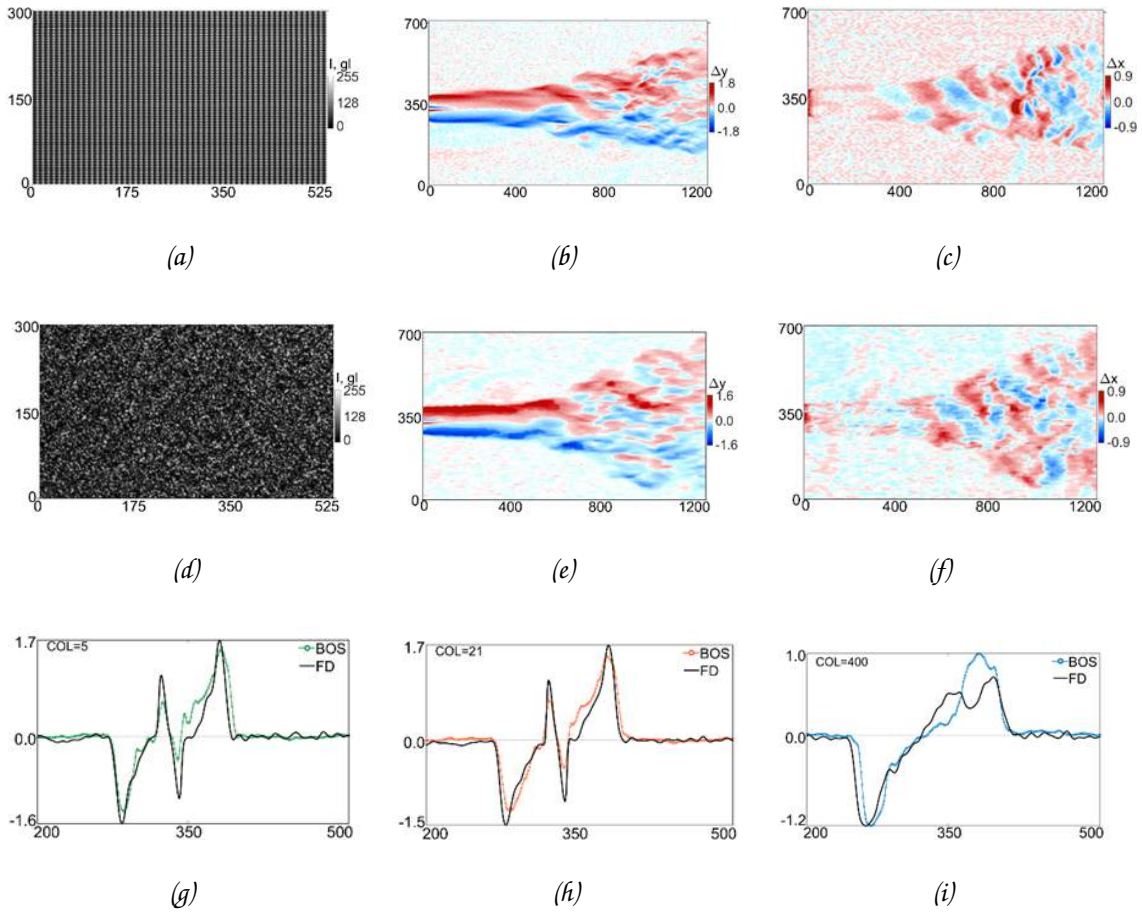

Fig. 4.1. Experimental results for gray-level images. (a) Raw image. (b) Δy-displacement map, (c) Δx-displacement map. BOS results: (d) Raw image, (e) Δy-displacement map (f) Δx-displacement map. Vertical cross sections of Δy-displacement maps [from (b) and (e)], for different columns: (g) 5, (h) 21 and (i) 400. Vertical axes in (g) - (i) show the displacements in pixels. Negative values are because the zero pixel was set at the center of the image. Horizontal axis in (a) - (i) are in pixels and represent a region of the image size.

which is analyzed in Sec. 2.2, since for this region; the equivalent number of pixels is four times the number used for the large region. The results for the smaller region of observation can then be used as the reference values of displacement.

In the previous results, a certain level of noise for FD is noticed throughout the image. To reduce that level of noise, the grating with crossed fringes is replaced by a grating with horizontal fringes (period of $4.9\ pix$), Fig. 4.2(a). The resulting y-displacement distribution is given in Fig. 4.2(b), and a typical BOS measurement in Fig. 4.2(c). In Figs. 4.2(d)-4.2(e), we report vertical cross sections of the y-component

of displacement for BOS and FD, as in Fig. 2.1.

When the object is smaller than the region of observation, for temperature measurement, it is not necessary to retrieve the two components of displacement. Since reference values of displacement for either a whole column or a whole row can be known in advance, and they can be used during the corresponding integration process; these known displacement values are generally associated with the temperature of the surrounding medium.

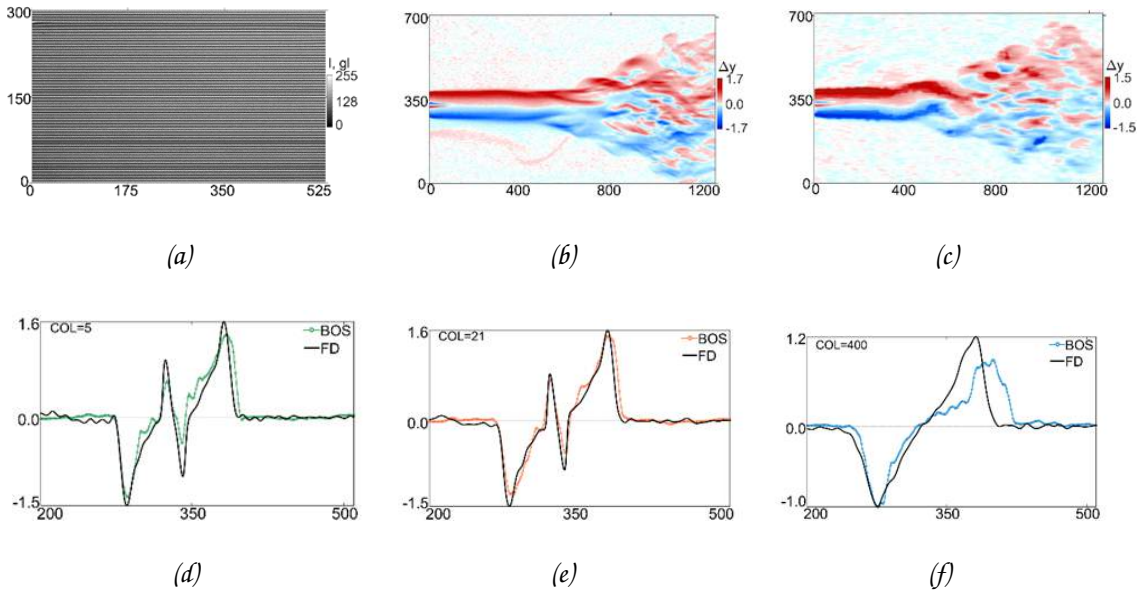

Fig. 4.2. Experimental results for gray-level images. (a) FD raw image (horizontal fringes). (b) FD Δy-displacement map, (c) BOS Δy-displacement map. Vertical cross sections of Δy-displacement maps [from (b) and (c)], for different columns: (d) 5, (e) 21 and (f) 400. Vertical axes in (d) - (f) show the displacements in pixels. Negative values are because the zero pixel was set at the center of the image. Horizontal axis in (a) - (f) are in pixels and represents a region of the image size.

For a better comparison between FD and BOS, their raw images are recorded simultaneously by encoding their respective spatial background images on different channels of color images, which are displayed by the Litemax monitor: the crossed grating is carried in the red signal of the RGB image and the randomly-located spot pattern in the green signal. Then, when the background is imaged –see Fig. 4.3(a), for example–, the two color-encoded backgrounds may be separated straightforwardly, as shown in Figs. 4.3(b) and 4.3(c), respectively. In this case, values for the periods of the fringes are $7.4\ pixels$

and $14.7\ pixels$, along the horizontal and vertical directions, respectively; the average particle diameter is $4\ pixels$.

In Figs. 4.3(d) and 4.3(e), the corresponding maps of the vertical component of displacement for FD and BOS re showed. In addition, for completeness, the horizontal component of displacement for BOS is presented in Fig. 4.3(f), which shows that the technique performance is maintained under the conditions of simultaneity.

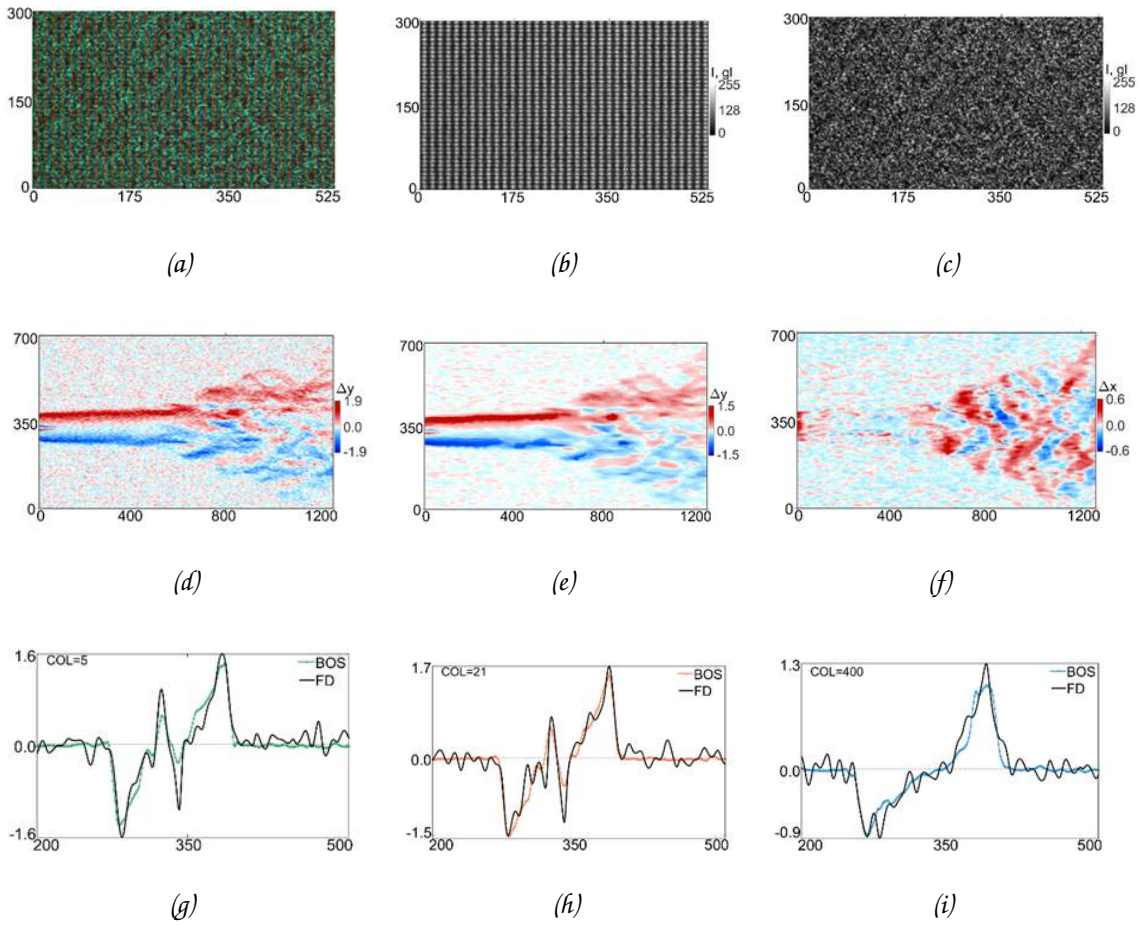

Fig. 4.3. Experimental results for RGB images. (a) Raw RGB image. (b) Red-channel image (FD image, crossed fringes), (c) Green-channel image (BOS image). (d) FD Δy-displacement map, (e) BOS Δy-displacement map, (f) BOS Δx-displacement map. Vertical cross sections of Δy-displacement maps [from (d) and (e)], for different columns: (g) 5, (h) 21 and (i) 400. Vertical axes in (g) - (i) show the displacements in pixels. Negative values are because the zero pixel was set at the center of the image. Horizontal axis in (a) - (h) are in pixels and represents a region of the image size.

Vertical cross sections of Figs. 4.3(d) and 4.3(e) are reported in Figs. 4.3(g)-4.3(i), and they represent data from different columns. These profiles show an increase in the level of noise with respect to the results displayed in Fig. 4.1. This effect is produced by the coupling effect among the three-color channels, which causes the presence of residual signals in the spatial information of the techniques. The fringe pattern is more affected by the high-frequency spot pattern, and therefore, the FD results report a higher level of noise. Despite this, FD's ability to detect large temperature gradients is preserved.

Additionally, it is observed that the BOS cross sections approximately follow the average curve of the FD cross sections. This means that BOS can yield partially correct values of displacement for zones with high-gradients of temperature, such as the depression formed at the exit of the nozzle.

By still considering the RGB technique variation, in order to decrease the noise level, the cross grating is replaced by a grating with horizontal fringes of period $7.4\ pixels$ –as shown in Fig. 4.4(a). In Fig. 4.7, figures similar to those in Fig. 4.3 are included. By comparing the results of Figs. 4.3 and 4.7, a slight reduction of noise can be observed in the latter figure.

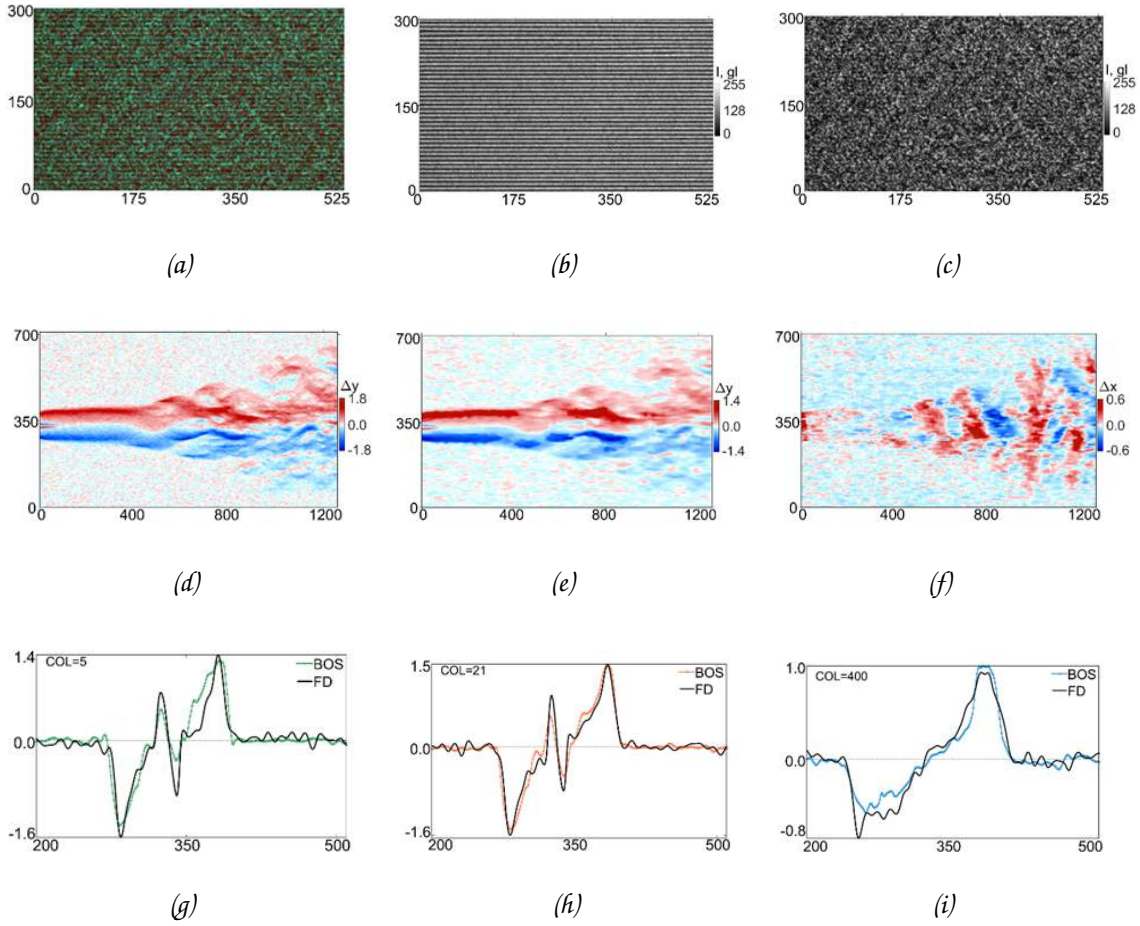

Fig. 4.4. Experimental results for RGB images. (a) Raw RGB image. (b) Red-channel image (FD image, horizontal fringes), (c) Green-channel image (BOS image). (d) FD Δy-displacement map for FD, (e) BOS Δy-displacement map, (f) BOS Δx-displacement map. Vertical cross sections of Δy-displacement maps [from (d) and (e)], for different columns: (g) 5, (h) 21 and (i) 400. Vertical axes in (g) - (i) show the displacements in pixels. Negative values are because the zero pixel was set at the center of the image. Horizontal axis in (a) - (i) are in pixels and represent a region of the image size.

4.1.2 Small region of observation

When the region of observation is reduced to $5.5 \times 10.5\ cm^2$, the level of noise for FD and BOS decreases with respect to the value obtained for the larger region (Sec. 4.1.1), as it is shown by comparing the results included in Figs. 4.5 and 4.1. The results reported in these figures lack simultaneity in the recording of the images of FD and BOS. In this case, grating periods of $9.7\ pixels$ and $18.8\ pixels$ was used for the horizontal and the vertical gratings, respectively. For BOS, a sub window of $16x32\ pixels$ is used, and the average particle diameter is $8\ pixels$. In Figs. 4.5(a) and 4.5(b) we present two typical raw images for each technique. In Figs. 4.5(c)-4.5(f), the associated Δy-displacement maps and vertical cross-sections for two different columns are shown.

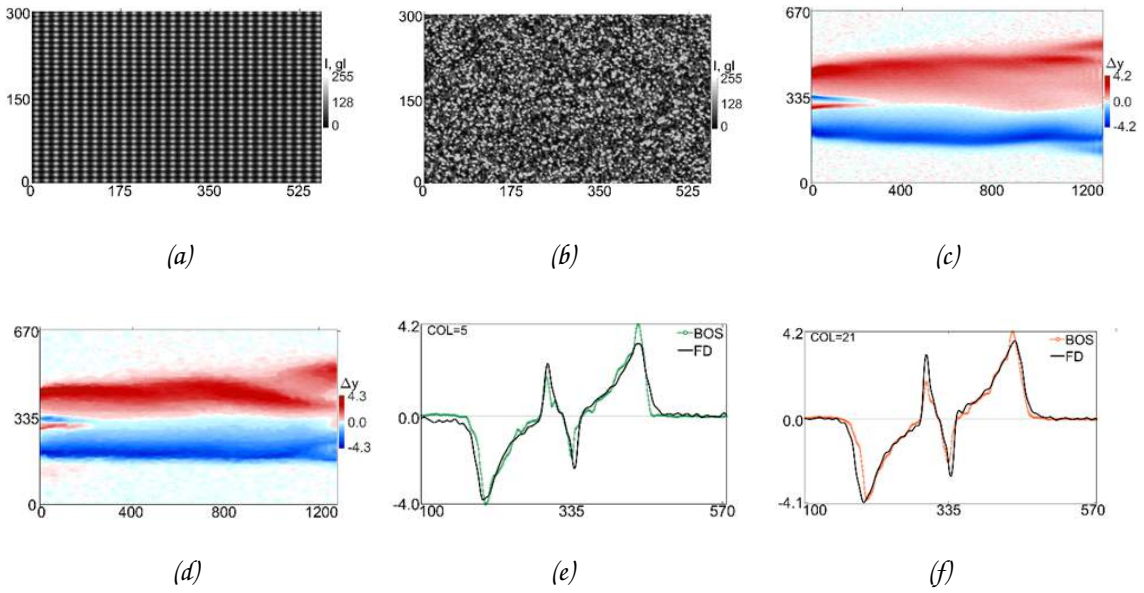

Fig. 4.5. Experimental results for gray-level images. Raw images: (a) FD, (b) BOS; Δy-displacement map for: (c) FD and (d) BOS. Vertical cross sections of Δy-displacement maps [from (c) and (d)], for different columns: (e) 5 and (f) 21. Vertical axes in (e) and (f) show the displacements in pixels. Negative values are because the zero pixel was set at the center of the image. Horizontal axis in (a) - (f) are in pixels and represent a region of the image size.

By taking into account the above smaller region of observation and using the color-encoded technique, results as those given in Fig. 4.5 can be obtained. In this case, the RGB image displayed by the Litemax monitor is composed of a grating with horizontal sinusoidal fringes, period of $9.7\ pixels$, encoded on the blue channel, and a field of randomly-located spots, encoded on the red channel. This RGB image serves as the background. A typical recorded image of the background is given in Fig. 4.6(a). Its red and blue components are displayed in Figs. 4.6(b) and 4.6(c), respectively. For this example, maps of the vertical component of displacement and some vertical cross sections are reported in Figs. 4.6(f) - 4.6(h). When comparing these cross sections with those of Fig. 4.5, we notice that the performance of both techniques remains almost unchanged. In addition, the FD's ability for detecting large gradients of temperature is slightly better than that of BOS. This performance dissimilarity was more evident for the larger region of observation, as shown in Sec. 2.3.

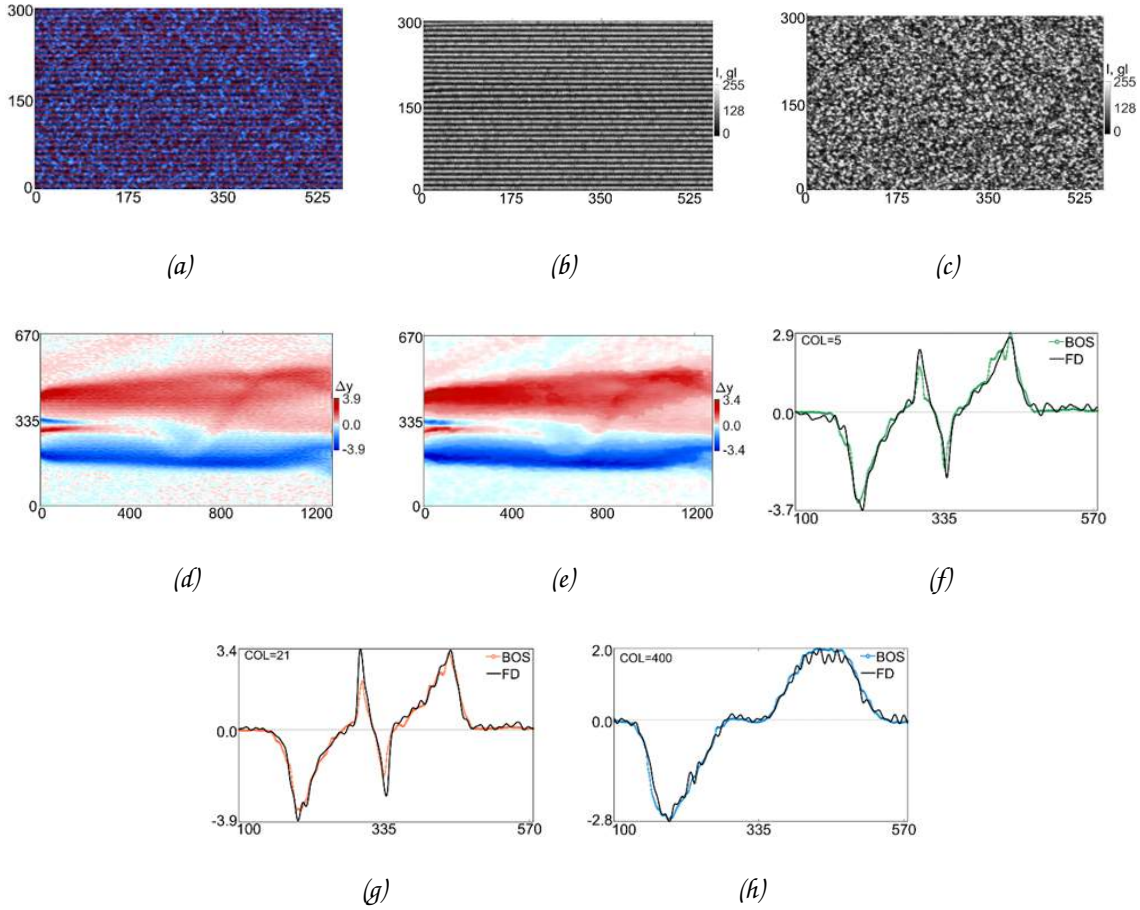

Fig. 4.6. Experimental results for RGB images. (a) Raw RGB image. (b) Red-channel image (FD image, horizontal fringes), (c) Blue-channel image (BOS image). (d) FD Δy-displacement map, (e) BOS Δy-displacement map, (f) BOS Δx-displacement map. Vertical cross sections of Δy-displacement maps [from (d) and (e)], for different columns: (f) 5, (g) 21 and (h) 400. Vertical axes in (f) - (h) show the displacements in pixels. Negative values are because the zero pixel was set at the center of the image. Horizontal axis in (a) - (h) are in pixels and represent a region of the image size.

4.2 Experimental evaluation. Sensitivity to blur

By considering the smaller region of observation, we induce blur in the recorded images by disturbing the hot jet issued by the nozzle. To achieve this, an auxiliary air jet is directed into the hot jet. The resulting changes in the temperature of the jet take place in times shorter than the exposure time of the camera ($30\ ms$). Also, because of turbulence effects, the induced changes in the jet do not hold between consecutive measurements. By considering this condition, typical RGB images as that in Fig. 4.7(a) can be registered. In this case, a crossed grating with periods of $9.5\ pixels$ and $12.4\ pixels$, along the horizontal and vertical directions was used, respectively. The blur is noticed on the separate images, Figs. 4.7(b) and 4.7(c). In Figs. 4.7(d) and 4.7(e), the vertical components of displacement for FD and BOS is displayed, respectively.

The effect of blur can also be seen from the vertical cross sections of Figs. 4.7(d) and 4.7(e), which are reported in Figs. 4.7(f)-4.7(h). From Fig. 4.7(f), it is observed that both techniques yield similar results, except for two narrow peaks, which are difficult for BOS to handle. Therefore, both FD and BOS can tolerate certain reduction of the contrast of the images. However, as the contrast is further reduced, the BOS cross sections do not follow the average of the FD curves. This suggests that BOS is more affected by zones with low contrast. Cross sections related to columns 10 and 513 show this effect. In these plots, zones largely affected by blur are indicated by letter A.

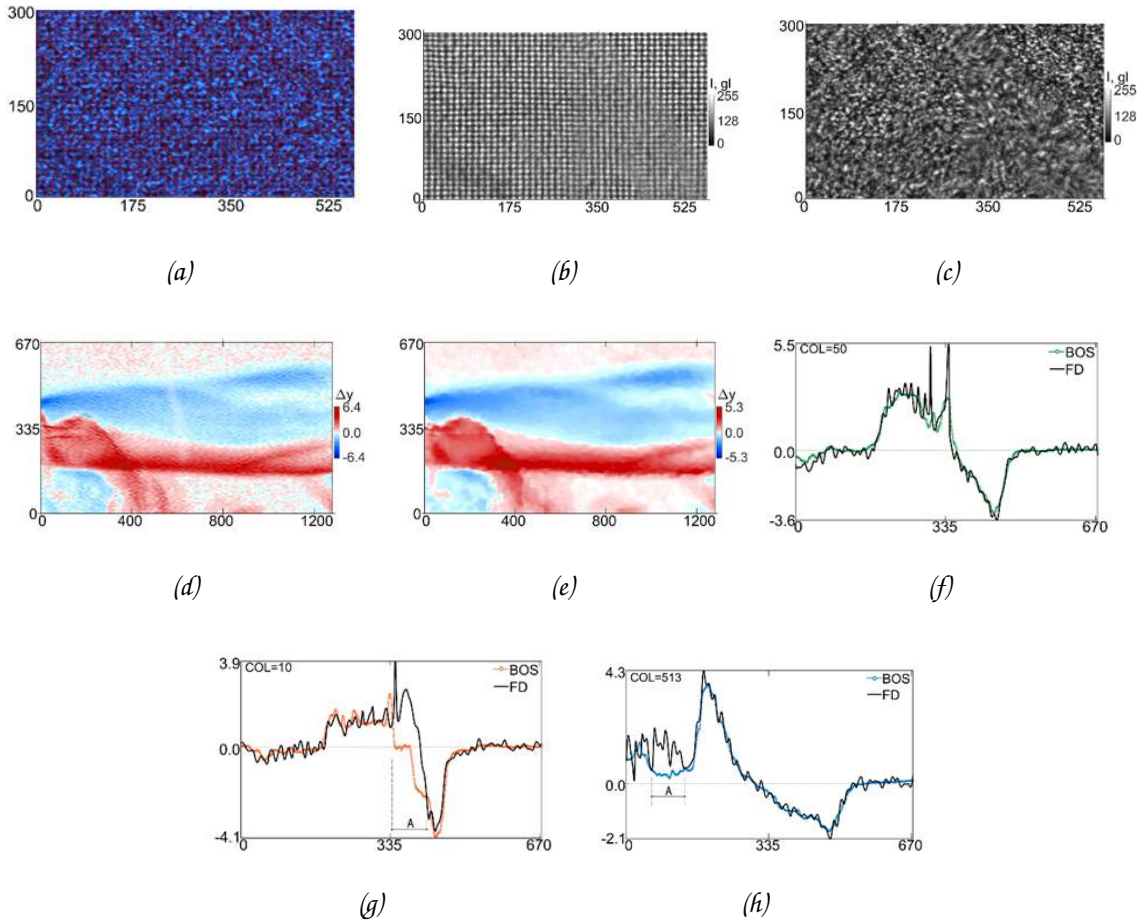

Fig. 4.7. Experimental results for blurred images. (a) Raw RGB image. (b) Red-channel image (FD image, crossed fringes), (c) Blue-channel image (BOS image). (d) FD Δy-displacement map, (e) BOS Δy -displacement map. Vertical cross sections of Δy -displacement maps [from (d) and (e)], for different columns: (f) 50, (g) 10 and (h) 513. Vertical axes in (f) - (h) show the displacements in pixels. Negative values are because the zero pixel was set at the center of the image. Horizontal axis in (a) - (h) are in pixels and represent a region of the image size.

4.3 Conclusions

By using the fringe deflection technique and the background-oriented schlieren, a series of experiments were conducted to measure temperature gradients of the jet generated by a gas burner. The formation of a small temperature depression in the jet allowed us to analyze qualitatively the spatial resolution of the techniques. In this regard, two different sizes of the region of observation were employed. BOS and FD were implemented either separately or simultaneously (this latter variation was carried out by encoding the signals for each technique on the RGB channels of color images). From the results, it is apparent that the performance of FD, considering spatial resolution, is slightly better than that of BOS. A similar result was found for images with low contrast.

Bibliography

[1] A. Blanco, B. Barrientos, and C. Mares, “Performance comparison of background-oriented schlieren and fringe deflection in temperature measurement: Part I. Numerical evaluation,” Opt. Eng. 55(5), 054102, 9pp (2016).

[2] A. Blanco, B. Barrientos, and C. Mares, “Performance comparison of background-oriented schlieren and fringe deflection in temperature measurement: Part II. Experimental evaluation,” Opt. Eng. 55(5), 054102, 9pp (2016).

[3] K. Hatanaka and T. Saito, “Background oriented schlieren method using multi-scale periodic pattern,” 29th International Symposium on shock waves 1, R. Bonazza and D. Ranjan, Eds., 453-458, Springer International Publishing, Switzerland (2015).

[4] P. Siegmann, V. Alvarez-Fernandez, F. Diaz-Garrido, and E. A. Patterson, “A simultaneous in- and out-of-plane displacement measurement method,” Opt. Lett. 36(1), 10-12 (2011).

[5] C. Mares, B. Barrientos, and A. Blanco, “Measurement of transient deformation by color encoding,” Opt. Express 19 (25), 25712–25722 (2011).

[6] L. F. Sesé, P. Siegmann, and E. A. Patterson, “Integrating fringe projection and digital image correlation for high quality measurements of shape changes,” Opt. Eng. 53(4), 044106, 9 pp (2014).

[7] F. Leopold, M. Ota, D. Klatt, and K. Maeno, “Reconstruction of the unsteady supersonic flow around a spike using the colored background oriented schlieren technique,” J. Flow Control, Meas. and Visualization 1(2), 69-76 (2013).

[8] M. Ota, K. Hamada, H. Kato, and K. Maeno, “Computed-tomographic density measurement of supersonic flow field by colored-grid background oriented schlieren (CGBOS) technique,” Meas. Sci. Technol. 22(10), 104011, 7 pp. (2011).

[9] Integrated Design Tools, Inc., ProVISION-XS PIV 3.12.01 Package, 2016, http://www.idtvision.com/products/software/provision/, (23 April 2016).

5

Application example: A Helmholtz resonator.

Contents

5.1 A Helmholtz resonator

In Chapter 2 was mentioned that Fringe Deflection (FD) is a technique capable of measuring ray deflections (or equivalently, projected refractive index gradients [1]) in two mutually orthogonal directions. The deflections field can be integrated to obtain the spatial distribution of the projected refractive index, which may be related to density [2]- [4] and concentration [5] variations, for example.

Due to its simplicity when compared with other schlieren methods, FD had used recently successfully in several applications of fluid dynamics [2]- [5].

In this section of the work, synthetic or zero-net mass jets are studied. A synthetic jet is produced by successive ejection and suction of fluid across an orifice. A movable diaphragm forming part of a sealed cavity typically generates the oscillatory flow.

Two adimensional numbers may characterize an unconfined synthetic jet flow [6]- [7]: the dimensionless stroke length $\frac{L_0}{d_o}$ and the Reynolds number $Re = \frac{U_0 d_0}{v}$. Where $L_0 = \int_0^{T/2} U(t)dt$ (length that a slug of fluid travels away from the orifice during the ejection portion of a period T), $U\,(t)$ is the spatially averaged velocity at the exit plane of the orifice, d_0 is the orifice hydraulic diameter, v is the kinematic viscosity of the fluid, $U_0 = \frac{L_0}{(T/2)}$. In addition, $\frac{L_0}{d_0}$ is inversely proportional to Strouhal number, since $f = 1/T$ the driving frequency. When the diaphragm and the cavity are driven into resonance, then the electrical power input is relatively low. This makes synthetic jets very efficient actuators for heat transfer, such as in thermal management of electronic devices.

The experimental setup consists of a Photron UX100 camera ($1280x1024\ pixels$), a printed sheet with sinusoidal fringes, with 25 fringes per centimeter, which acts as the reference background, and an imaging Canon lens with focal distance of $300\ mm$ (working at $f\#16$). The printed background is located at a distance $d^{'} = 5170\ mm$ from the camera, and the synthetic air jet is placed at a distance $D = 600\ mm$ from the background. Both background and object plane are positioned within the depth

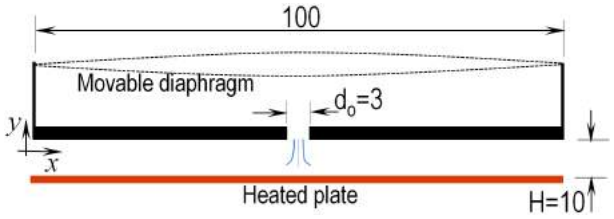

Fig. 5.1. Synthetic air jet generator. H is the distance between the heated plate and the cavity surface. Dimensions are in mm.

of focus of the lens. For the camera, images are acquired at $2000\ fps$. A schematic diagram of the device for producing the synthetic air jet is shown in Fig. 5.1. The orifice diameter is $3\ mm$ and its stream wise length is $6.31\ mm$.

The region of observation is $10x100\ mm^2$ for full images. However, for presenting the results the images are clipped. A speaker driven by a sinusoidal signal generates the airflow. The background is illuminated by a $2x10$ matrix of high power LEDs (3 W each). The background is printed on a transparent slide and placed over the surface of an acrylic sheet.

The Reynolds number and the adimensional stroke length of the synthetic air jet are set to 520 (which implies laminar flow) and 4.4 (which in turn accomplishes the condition for jet formation [8]), respectively. The driving frequency of the speaker matches the first resonance cavity frequency, $125\ Hz$. The heated surface ($80\ ^oC$) corresponds to the aluminum plate of a programmable temperature device (Model Echotherm IC30, Torrey Pines Scientific).

The reference object state relates to the convective plume produced by the surface at $80\ ^oC$. A uniform temperature distribution along the plate surface is obtained, Fig. 5.2(d). The displaced images are in turn registered with the speaker turned on. Figure 5.2(a) shows a typical FD image for the air jet.

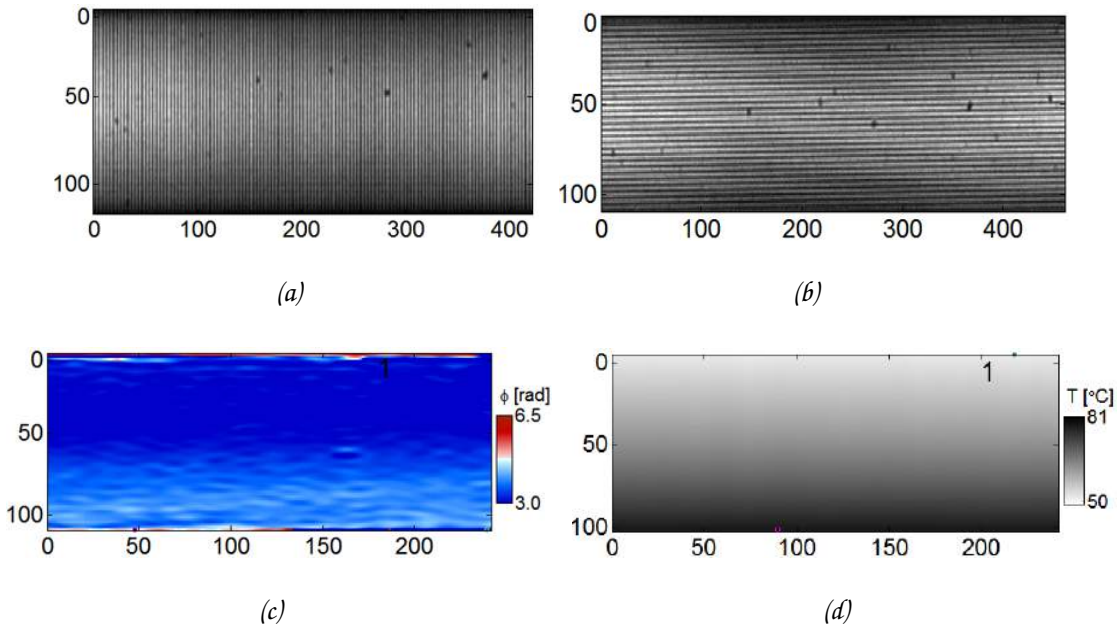

Fig. 5.2. Typical images of FD for (a) the synthetic air jet (the observation region is $10 \times 36\ mm^2$) and (b) the convective plate with no jet. The corresponding phase map and temperature field of (b); (c) and (d), respectively. Axis are in pixels.

Fringe displacements are calculated by the Fourier method [8]. When the aluminum plate is heated, the resulting time-series displacement maps for one and a half cycles of the jet are shown in Fig. 5.3. One cycle of the system comprises 16 images. The first half of the sequence of images of a cycle starts with the forward movement of the diaphragm, which produces the ejection of air. At the 9th image from the onset of the ejection period, the synthetic jet reaches the heated plate and interacts with it. By considering these data, an approximated average speed of $3.3\ m/s$ is calculated for the air jet. The ejected jet forms a vortex pair at the exit of the cavity. The vortices move downstream, and before reaching the hot plate, they lose their coherence (image 12) and become turbulent. In images 9-16, we can see that the jet interacts with the plate and at the same time air is drawn into the cavity. At the hot plate surface, we notice an enhanced mixing of the spatial structures arising from the breakdown of the vortex rings that impinge on the plate [9]. From image 17, a new cycle starts, and another jet is created. This jet interacts with the previous one and enhances the mixing process.

By considering the time series phase maps, it is noticed that for the first cycle, it takes 9 images for the get to reach the heated plate and only 6 for the second cycle. We think that this discrepancy stems from the fact that the first cycle corresponds to the moment at which the speaker is turned on and apparently the systems takes some time to respond. At later cycles, the full periodicity of the phenomenon is observed.

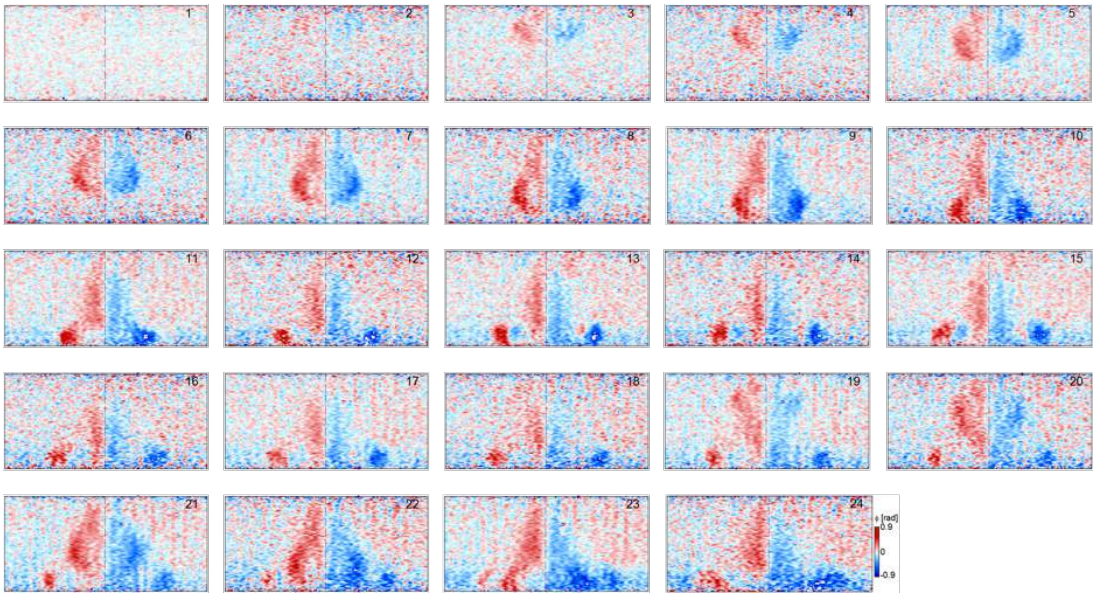

Fig. 5.3. Phase maps corresponding to a complete cycle of the resonator. The image size is $116x201\ pix$. *The color map denotes phase values in the range* -0.9 *to* $0.9\ rad$.

The jet dynamics can be optionally shown by the associated temperature fields. By considering that the variation of the index of refraction is axisymmetric and modeled as a Gaussian function of (y, z), then Eq. 2.6 can be simplified to

$$\frac{\partial n}{\partial x} = \frac{n_0 \Delta x(x, y)}{s\ell}, \tag{5.1}$$

where ℓ is the equivalent width of the jet and is related to the diameter of the jet, d_j, as $\sqrt{\pi} d_j/2$. As pointed out [10], the jet diameter can be modeled as a function of the stream wise length,y. This parameter is estimated by measuring the span wise length of the jet for each instant. Then, maps of the change of the refractive index can be obtained by any integration method from the displacement distribution; here the trapezoidal method along the x-direction was used [11]. When integration is performed, the initial values of the variation of refractive index (values from first column), are set to zero. Eq. 2.8 ob-

tains temperature values. As it is noticed, the reference temperature at each point, T_0, is needed. These can be known by measuring the temperature field resulting from comparing images without convective plume (heated plate turned off, ambient temperature of $20\ ^oC$) and with convective plume (heated plate set at $80\ ^oC$). For this latter case, an horizontal grating was used, and for the variation of the refractive index $\partial n/\partial y = n_0 \Delta y/(s\ell_P)$, where $\ell_P$is the length of the heated plate along the observation direction, $12.5\ cm$. The integration process is done along the vertical direction, where the values of temperature at the heated plate are assumed to be $80\ ^oC$ and the corresponding values for n_0, 1.000186. A second value of temperature is necessary for the reference temperature distribution to be estimated; this value is measured by a thermocouple located at the bottom surface of the cavity and is $52\ ^oC$. The corresponding phase map and temperature fields for this reference measurement are shown in Figs. 5.2(c) and 5.2(d).

Considering the reference temperature measurement described and the phase maps of Fig. 5.3, the resulting temperature maps of the synthetic jet are obtained and are given in Fig. 5.4. The production of a synthetic jet in each cycle is clearly seen. The temperature image 1 shows the onset of the ejection of the jet, which is embedded in a varying temperature distribution, which coincides with that shown in Fig. 5.2(d). As is noticed, the synthetic jet transports air which is basically at the temperature observed at the exit of the cavity. As this cool air gets close to the heated plate it becomes warmer, image 9. After impinging with the plate (images 10-17), it is observed a further decrease of the jet temperature. As mentioned previously, in image 17 a new ejection period begins and the new jet starts interacting with the debris of the previous jet. The results shown by the times series agrees with the expected phenomenon: the synthetic jet entrains cool air from ambient, impinges on the bottom heated plate surface and circulates the surrounding air back to the ambient.

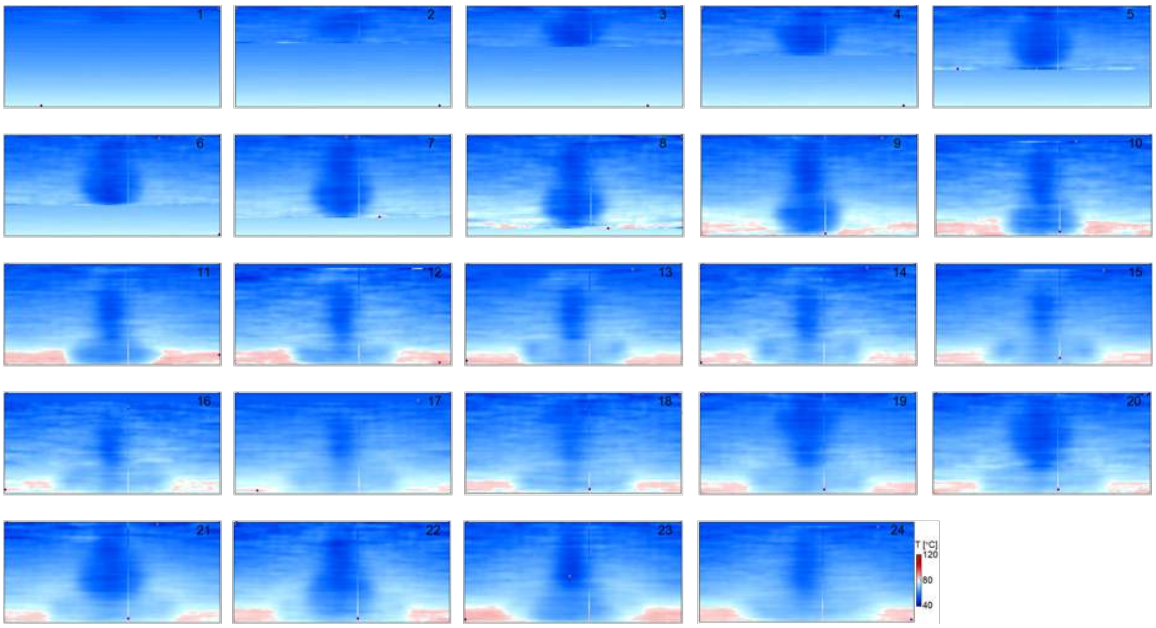

Fig. 5.4. Temperature distribution maps corresponding to Fig. 5.3. The image size is $116 \times 201\ pixels$*. The color map denotes temperature values in the range* $40\ ^oC$ *to* $120\ ^oC$*.*

5.2 Conclusions

The FD technique has been applied to the measurement of temperature of a synthetic air jet when interacting with the thermal flow produced by a heated surface. The results show the production of a synthetic air jet by a Helmholtz resonator and the subsequent motion downstream, this occurring during about half the cycle of the driving frequency. In the other half of the period, the air jet interacts with the heated plate and draws away surrounding warmed air.

Despite the region of interest was relatively small in the vertical direction, $1\ cm$, the results show that FD can be potentially used for the analysis of this type of devices [12].

Bibliography

[1] B. S. Dalziel, G. O., Hughes, and B. R., Sutherland, “Whole-field density measurements by synthetic schlieren”, Exp. Fluids 28, 322-335pp., (2000).

[2] H., Richard, and M., Raffel, “Principle and applications of the Background Oriented Schlieren (BOS) method”, Meas. Sci. Tech. 12, 1576-1585pp., (2001).

[3] J., Hazewinkel, L. R. M. Maas, and S. B., Dalziel, “Tomographic reconstruction of internal wave patterns in a paraboloid”, Exp. Fluids 50, 247-258pp., (2011).

[4] G. E., Elsinga, B. W., Oudheusden, F., Scarano, and D. W., Watt, “Assessment and application of quantitative schlieren methods: Calibrated color schlieren and background oriented schlieren”, Exp. Fluids 36, 309-325pp., (2004).

[5] G. E. A., Meier, “Computerized background-oriented schlieren”, Exp. Fluids 33, 181-187pp., (2002).

[6] T., Persoons, and T. S., O’Donovan, “A pressure-based estimate of synthetic jet velocity”, Physics of Fluids 19, 128104-1 (2007).

[7] A., McGuinn, T., Persoons, T. S., O’Donovan, P., Valiorgue, and D. B., Murray, “Heat transfer measurements of an impinging synthetic air jet with constant Stroke length”, 5th European Thermal-Sciences Conference, The Netherlands, (2008).

[8] M., Takeda, H., Ina, and S., Kobayashi, “Fourier-transform method of fringe-pattern analysis for computer-based topography and interferometry”, JOSA A72 (1), 156-160pp., (1982).

[9] U., Ingard, "On the theory and design of acoustic resonators", J. Acoust. Soc. Am., 25(6), 1037-1061pp., (1953).

[10] B. L., Smith, and A., Glezer, "The formation and evolution of synthetic jets", Phys. Fluids, 10(9), 2281-2297pp., (1998).

[11] J., Davis, Philip, Rabinowitz, "Methods of Numerical Integration", Academic Press Inc., New York, 51-52pp., (1984).

[12] A. Blanco, B. Barrientos, A. J. Moore, and C. Mares, "Temperature measurement of a synthetic air jet produced by a Helmholtz cavity", Emerging Challenges for Experimental Mechanics in Energy and Environmental Applications, Proceedings of the 5th International Symposium on Experimental Mechanics and 9th Symposium on Optics in Industry (ISEM-SOI), Springer International Publishing, ISBN: 978-3-319-28513-9 doi:10.1007/978-3-319-28513-9, (2016).

6

General Conclusions and Future Work

Contents

6.1 Discussions

Previous works have dealt with the problem of analyzing the performance of BOS [1]- [3]. To improve the accuracy of the technique, they also used color codification: three speckle patterns were codified in the signals of each color channel of an RGB projector. A Bayer sensor camera recorded images of the projected images and 8 independent images were produced: three images with pure primary colors (RGB), three images with primary colors, an image with secondary colors, and a black-and-white thresholded image. When the results from each independent image were averaged, the accuracy was benefited.

In [4]- [5], the three speckle patterns were replaced by two color-encoded gratings, one coded in the red signal and the other in the blue signal of the background image. The two gratings are perpendicular to each other to have sensitivity of index of refraction change along mutually perpendicular directions. The two techniques, with colored grating and colored spots, are compared by measuring the density distribution of a supersonic flow. They report that the spatial details of the studied phenomena are captured more sharply through the technique that uses the colored gratings.

However, in these works, two of the main characteristics that affect the accuracy of BOS, spatial resolution and robustness to blur and low-contrast, were not analyzed, as it has been done in the present work.

6.2 Conclusions

A comparison between the performance of BOS and FD has been shown when used for temperature measurement. The comparison was carried out just for the determination of displacement maps, since from that point on wards, the processing is exactly the same for the two techniques.

Both techniques are variations of the schlieren technique, where a knife usually is used to reveal ray deflections. In BOS and FD, the knife is replaced by a background image.

The processing time for the two techniques is similar. However, in FD, if care is taken to not allow the phase to get wrapped, then FD is more efficient; besides, generally grating images in FD contain relatively low levels of noise, so they can be processed by using a simple unwrapping algorithm.

When the distribution of the change of index of refraction can be approximated by a Gaussian function, then the projected variation of the optical path corresponds to exactly the latter Gaussian function. Therefore, when the measured displacement maps show a variation that can be adjusted to the derivative of a Gaussian function, then the refractive index change is recovered straightforwardly, avoiding the use of any deprojection method (for example, Abel integrals) and even the use of any integration algorithm.

Another important result is that FD, overall, presents slightly higher accuracy than BOS, in particular when images with blur and low-contrast are used. For industrial applications, however, both techniques deliver acceptable results (with uncertainties of approximately 5%).

Another important conclusion that was drawn from this work is that FD´s resolution is sufficiently high as to produce results even for quite small variations of index of refraction, such as those caused by the presence of an air jet. This issue was particularly observed in the practical case of the analysis of a Helmholtz cavity, where a synthetic jet of air is formed. In this case, the performance of FD was highly

demanded, since the contrast of the images was relatively low —due to the short exposure times of the high-speed camera, and the transiency of the dynamics of the event relatively large (the size of the jet was only $1\ cm$).

Some important parameters of the techniques are the following:

- *Accuracy of displacement calculation:* 1% *of the measured range.*
- *Spatial resolution:* $0.1\ mm$.
- *Resolution of index of refraction change:* 10^{-6}.
- *Resolution of density change:* $10^{-3}\ kg/m^3$.
- *Resolution of temperature change:* $1\ ^oC$.
- *Range of object size: From* $1\ mm$ *to* $1\ m$.
- *Range of temperature: From* $20\ ^oC$ *to* $1700\ ^oC$.
- *Range of displacements: From* $0\ m$ *to* $2.4x10^{-5}\ m$.
- *Range of deflection angles: From* $0\ rad$ *to* $3.4x10^{-4}\ rad$.
- *Range of density: From* $1.202\ kg/m^3$ *to* $0.215\ kg/m^3$
- *Range of values of periods in FD:* $5.2x10^{-4}\ m$ *to* $1.6x10^{-3}\ m$.
- *Range of values of spot diameters in BOS:* 2 *to* $4\ pixels$.
- *Range of values of sub images in BOS:* $16x16$ *to* $128x128\ pixels$.
- *Range of values of the focal distance of the imaging lens:* $70 - 210\ mm$.

6.3 Future Work

Future work comprises combining the results obtained by FD in the Helmholtz cavity with those produced by Particle Image Velocimetry (PIV), in order to complement the temperature results with those of velocity. The larger the number of variables known for the dynamics of an event, the better the description of its spatial and temporal behavior.

Another part of the future work is the use of these optical techniques for obtaining temperature fields in the drum of an electric dryer, which may allow us to have insights related with the increase of energy efficiency.

Another point to be studied is the way to increase the resolution of FD for the study of transient phenomena, where a high-speed camera is employed. Currently, we have used arrays of 5-W LEDs as the source of illumination, but, since LEDs with larger power have recently appeared in the market, they may be used instead.

A final topic to be analyzed is the way to increase the depth of field of the imaging system, as the object and the background have to be simultaneously in focus. This may be dealt with by using light field cameras.

6.4 List of products derived from this work

Published papers

(1) A. Blanco, B. Barrientos, and C. Mares, "Performance comparison of background-oriented schlieren and fringe deflection in temperature measurement: Part I. Numerical evaluation", Opt. Eng. 55(5), 054102, 9pp (2016).

(2) A. Blanco, B. Barrientos, and C. Mares, "Performance comparison of background-oriented schlieren and fringe deflection in temperature measurement: Part II. Experimental evaluation", Opt. Eng. 55(5), 054102, 9pp (2016).

(3) C. Mares, B. Barrientos, and A. Blanco, "Measurement of transient deformation by color encoding," Opt. Express 19 (25), 25712–25722 (2011).

Papers in preparation

(1) A. Blanco, B. Barrientos, A. Moore and C. Mares, "Temperature measurement of a Synthetic Jet produced by a Helmholtz Cavity: qualitative and quantitative description"

Full works in congresses

(1) A. Blanco, B. Barrientos, and C. Mares, "Temperature measurement of a Synthetic Jet produced by a Helmholtz Cavity", 5th International Symposium on Experimental Mechanics, Guanajuato, Gto. México, 2015.

(2) A. Blanco, B. Barrientos, and C. Mares, "Medición de temperatura en el tambor de una secadora de ropa mediante deflexión de franjas", XXVI Reunión Anual de Óptica; Universidad de Sonora; Hermosillo, Sonora, México: 2013.

(3) A. Blanco, B. Barrientos, and C. Mares, “Análisis simultáneo en la sensitvidad y precisión de las técnicas de deflexión de franjas y schlieren de fondo orientado para la medición de temperatura mediante codificación a color”, LV Congreso Nacional de Física; Universidad de Morelia; Morelia, Michoacán, México: 2012.

(4) A. Blanco, B. Barrientos, and C. Mares, “Comparison of Background Oriented Schlieren and Fringe Deflection in temperature measurement”, 22nd General Congress of the International Comission for Optics ICO; Benemérita Universidad Autónoma de Puebla; Puebla, Puebla, México: 2011.

Proccedings

(1) A. Blanco, B. Barrientos, and C. Mares, “Comparison of Background Oriented Schlieren and Fringe Deflection in temperature measurement”, SPIE Vol. 8011, 801180; doi:10.1117/12.903403, 2011.

(2) A. Blanco, B. Barrientos, A. J. Moore, and C. Mares, "Emerging Challenges for Experimental Mechanics in Energy and Environmental Applications, Proceedings of the 5th International Symposium on Experimental Mechanics and 9th Symposium on Optics in Industry (ISEM-SOI)", Springer International Publishing, ISBN: 978-3-319-28513-9 doi:10.1007/978-3-319-28513-9, 2016.

Visiting stays

(1) Department of Mechanical Engineering, School of Engineering and Physical Sciences, Heriot – Watt University, Edinburgh. April - May 2012.

Bibliography

[1] F. Leopold, M. Ota, D. Klatt, and K. Maeno, “Reconstruction of the unsteady supersonic flow around a spike using the colored background oriented schlieren technique”, J. Flow Control, Meas. and Visualization 1(2), 69-76 (2013).

[2] F. Leopold, “The Application of the Colored Background Oriented Schlieren Technique (CBOS) to Free-Flight and In-Flight Measurements” Journal of Flow Visualization and Image Processing, 16(4), pp. 279-293, (2009).

[3] F. Leopold, J. Simon, D. Gruppi and H. J. Schäfer, “Recent Improvements of the Background Oriented Schlieren Technique (BOS) by Using a Colored Background”, 12th International Symposium on Flow Visualization, Göttingen, 10 p. (2006).

[4] M. Ota, K. Hamada, H. Kato, and K. Maeno, “Computed-tomographic density measurement of supersonic flow field by colored-grid background oriented schlieren (CGBOS) technique”, Meas. Sci. Technol. 22(10), 104011, 7 pp. (2011).

[5] M. Ota, F. Leopold, F. Jagusinski, and K. Maeno, “Comparison between CBOS (Colored Background Oriented Schlieren) and CGBOS (Colored-Grid Background Oriented Schlieren) for Supersonic Flow”, 15th International Symposium on Flow Visualization, ISFV15, 8 pp., (2012).